

NATIONAL AERONAUTICS AND SPACE ADMINISTRATION • WASHINGTON, D. C. • MAY 1977

for Langley Research Center

Wichita, Kans. 67208

WICHITA STATE UNIVERSITY

Prepared by

*H. C. Seebaram and W. H. Wentz, Jr.*

A LOW SPEED TWO-DIMENSIONAL STUDY  
OF FLOW SEPARATION ON THE GA(W)-1 AIRFOIL  
WITH 30-PERCENT CHORD FOWLER FLAP

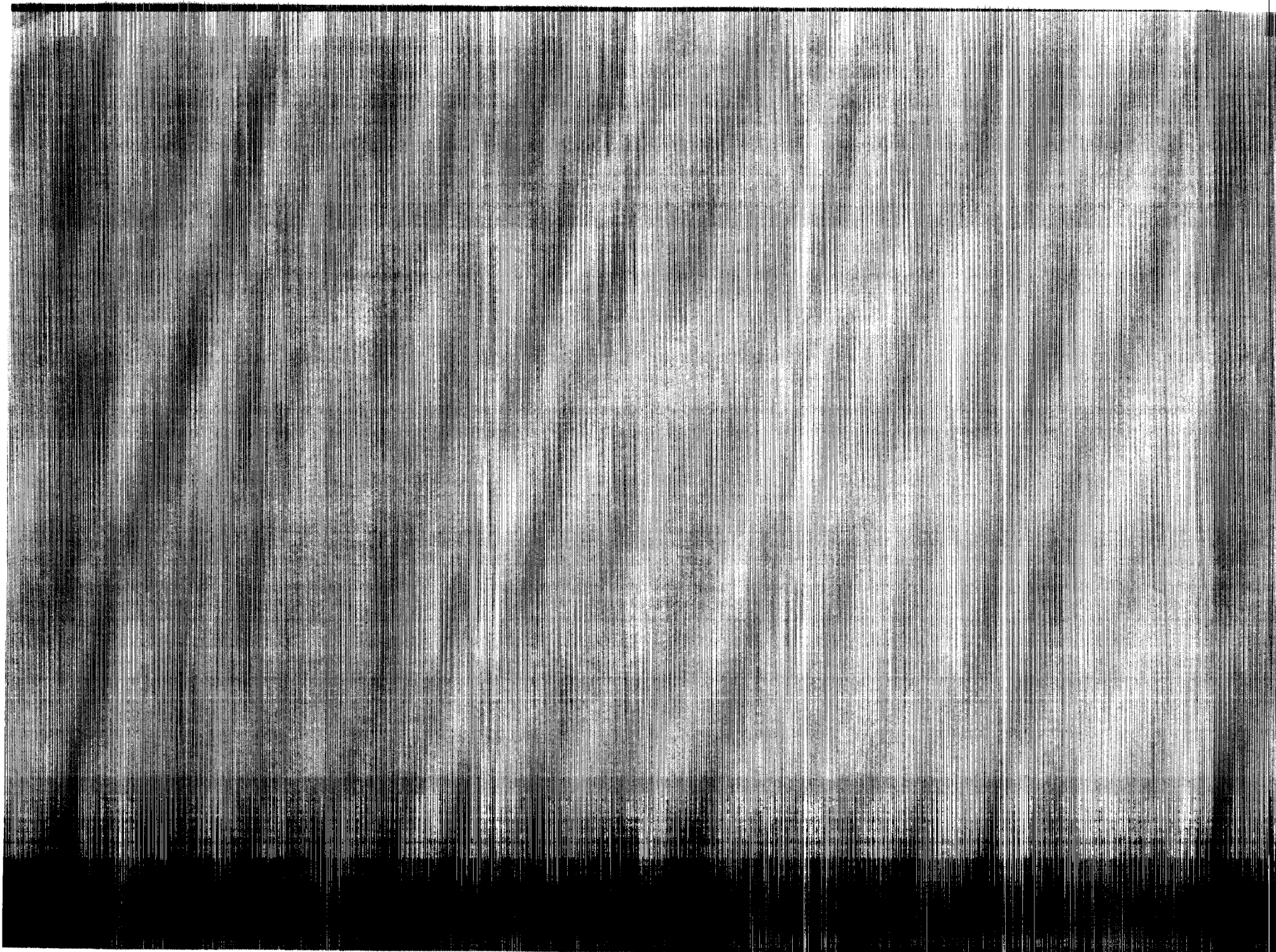
NASA CR-2844

REPORT

NASA CONTRACTOR

NASA CR-2844





1. Report No. NASA CR-2844	2. Government Accession No.	3. Recipient's Catalog No.	
4. Title and Subtitle A Low Speed Two-Dimensional Study of Flow Separation on the GA(W)-1 Airfoil With 30-Percent Chord Fowler Flap.		5. Report Date May 1977	6. Performing Organization Code
		8. Performing Organization Report No.	
7. Author(s) H.C. Seetharam and W. H. Wentz, Jr.		10. Work Unit No.	
9. Performing Organization Name and Address Wichita State University Wichita, Kansas 67208		11. Contract or Grant No. NGR 17-003-021	
		13. Type of Report and Period Covered Contractor Report	
12. Sponsoring Agency Name and Address National Aeronautics & Space Administration Washington, D. C. 20546		14. Sponsoring Agency Code	
		15. Supplementary Notes Langley Technical Monitor: Kevin W. Noonan Topical Report	
16. Abstract <p>Experimental measurements of flow fields with low speed-turbulent boundary layers have been made for the GA(W)-1 airfoil with a 0.30c Fowler flap deflected 40° at angles of attack of 2.7°, 7.7°, and 12.8°, at a Reynolds number of <math>2.2 \times 10^6</math>, and a Mach number of 0.13. Details of velocity and pressure fields associated with the airfoil-flap combination are presented for cases of narrow, optimum and wide slot gaps. Extensive flow field turbulence surveys were also conducted employing hot-film anemometry. For the optimum gap setting, the boundaries of the regions of flow reversal within the wake were determined by this technique for two angles of attack. Local skin friction distributions for the basic airfoil and the airfoil with flap (optimum gap) were obtained using the razor-blade technique.</p>			
17. Key Words (Suggested by Author(s)) Flow Separation GA(W)-1 Airfoil with Flower Flap Lowspeed Turbulent Boundary Layers		18. Distribution Statement Unclassified - Unlimited  Subject Category 02	
19. Security Classif. (of this report) Unclassified	20. Security Classif. (of this page) Unclassified	21. No. of Pages 71	22. Price* \$4.50



A LOW SPEED TWO-DIMENSIONAL STUDY OF  
FLOW SEPARATION ON THE GA(W)-1 AIRFOIL  
WITH 30-PERCENT CHORD FOWLER FLAP

Summary

Experimental measurements of flow fields with low speed-turbulent boundary layers have been made for the GA(W)-1 airfoil with a 0.30c Fowler flap deflected  $40^\circ$  at angles of attack of  $2.7^\circ$ ,  $7.7^\circ$ , and  $12.8^\circ$ , at a Reynolds number of  $2.2 \times 10^6$ , and a Mach number of 0.13. Details of velocity and pressure fields associated with the airfoil-flap combination are presented for cases of narrow, optimum and wide slot gaps. Extensive flow field turbulence surveys were also conducted employing hot-film anemometry. For the optimum gap setting, the boundaries of the regions of flow reversal within the wake were determined by this technique for two angles of attack. Local skin friction distributions for the basic airfoil and the airfoil with flap (optimum gap) were obtained using the razor-blade technique.

The results of this investigation indicate that with an optimum gap, the airfoil lower surface boundary layer and the flap upper surface boundary layer at the slot exit are separated by a constant energy core of finite width. This core flow vanishes near the mid-flap chord location. Local skin friction measurements on the basic airfoil compare favorably with theoretical values where the flow is attached at pre-stall angles of attack. Measurement difficulties were encountered with pressure-type instruments in regions of high turbulence. In these regions the hot-film anemometer provided meaningful data. It is recommended that studies of this type be conducted for intermediate flap settings, and for new airfoils of greater thickness.

## INTRODUCTION

Significant progress has been achieved during this decade in the state of the art of computational fluid mechanics related to airfoils. Highly sophisticated computational routines are now available to account for the interactions between potential and viscous flows associated with single- and multi-element airfoils (for example, Reference 1). The theoretical model of Reference 1 works reasonably well for multi-element airfoils when the flow is attached and flap deflections are small (Reference 2). However, this theoretical model fails to simulate regions of reversed flow on the airfoil and the flap (or vane(s)) and in the wake. The theoretical model employs subroutines for slot flow and confluent boundary layer analyses which also have the following limitations:

1. The slot geometry is assumed to exhibit a smooth continuous area distribution with no flow separation. Many practical construction wing-flap systems have abrupt contour changes in the flap cove, with separation and reattachment ahead of the slot. Limited lower surface flow studies carried out during the research reported in Reference 2 indicate separation and reattachment even for a fairly smooth flap cove geometry.

2. In order to have a definable slot, the flap overlap must be at least  $0.01c$ . Practical configurations exist which do not meet this requirement.

3. A semi-empirical method based on a limited set of experimental data is employed to define the pressure distribution throughout the slot region.

4. In the region of the confluence of the boundary layers of airfoil and flap with the slot flow, the maximum velocity must be equal to, or greater than, the velocity at the outer edge of the confluent boundary layer. Also restrictions on the values of streamwise gradients of non-dimensional maximum velocity and wake velocity are imposed. These restrictions are based on fully attached flow conditions on both airfoil and flap. But at angles of attack near stall the flap flow can be attached, and separation can be present over the aft portion of the main airfoil (Reference 2). In such cases it is probable that these limits have been exceeded.

Previously reported work does not provide all the types of data needed to eliminate the limitations of the mathematical model of Reference 1. Experimental work reported in Reference 3 is concentrated on the flow around an airfoil with a single slotted flap. The report contains data for two specific flap deflections of  $10^\circ$  and  $30^\circ$ , with various flap gap settings at pre-stall angles of attack. An extension of this work was carried out by Ljungström (Reference 4), in which details of the flow around an airfoil with multiple slotted flaps were obtained. The flap deflections

were again limited to  $30^\circ$  and only pre-stall angles of attack were considered, with various flap gap settings. The results of References 3 and 4 emphasize mainly determining the flow conditions which exist at optimum flap gap and positive overlap of greater than .01c. The choices of pre-stall angles of attack and flap deflection appear to have been made to insure attached flow conditions on airfoil and flap. Extensive total pressure surveys at the slot exit and on the flap were carried out mainly to study the influence of the wing wake on the boundary layer development on the flap. A qualitative description of the flow mechanism and performance characteristics of an airfoil-flap combination is given by Smith (Reference 5). While Smith's paper deals with the gross effects of mutual viscous and inviscid interactions of multi-element airfoils, details of confluent boundary layer development over the flap have not been completely discussed. Also, none of the above three works discuss the details of wake development associated with airfoil and flap.

The present investigation was undertaken to determine the pressures and velocities in the external flow field, at the slot exit, in the confluent boundary layer, and in the wake of a two-component airfoil with attached and separated flow conditions to aid the future formulation of an improved (relative to Reference 1) mathematical model for multi-component airfoils. The GA(W)-1 airfoil with a 0.30c Fowler flap was selected for this investigation because a complete set of force data had been measured and reported (Reference 2) on this configuration and this airfoil was of considerable interest to the general aviation community.



The flap deflection angle of  $40^\circ$  was selected for the present investigation because at the optimum gap setting this deflection had resulted in the highest maximum lift coefficient for this configuration. The optimum setting for the  $40^\circ$  flap deflection from the two-dimensional tests (Reference 2) was found to have a gap of  $0.027c$  and an overlap of  $-.007c$ . However, during the design for the Advanced Technology Light Twin Aircraft (Reference 6), Robertson Aircraft Company suggested a gap of  $.03c$  with zero overlap to simplify flap track fabrication. This configuration was evaluated and a comparison is shown in Figure 1. In view of the good agreement between the two flap settings, the  $.03c$  gap with zero overlap was chosen for the present tests.

Three angles of attack ( $2.7^\circ$ ,  $7.7^\circ$ ,  $12.8^\circ$ ) representing three distinct flow patterns observed on this configuration during tuft studies (Reference 2) were chosen for the current evaluation. These flow patterns are the following:

- (1) At low angles of attack (up to  $2.7^\circ$ ), a shallow region of separation is present at the flap trailing edge.
- (2) The flap separation decreases with increasing angle of attack and the flap is attached at  $7.7^\circ$ . At higher angles of attack, through stall ( $\alpha = 10.3^\circ$ ) separation appears and progresses upstream on the main airfoil.

- (3) At the post-stall ( $\alpha \geq 12.8^\circ$ ) angles of attack the region of separation continues to progress forward towards the leading edge of the main airfoil with the flow remaining attached on the flap.

#### SYMBOLS

To the maximum extent possible, physical measurements are presented in the non-dimensional form. Where dimensional quantities are required, they are given in both International (SI) Units and U.S. Customary Units. Measurements were made in U.S. Customary Units. Conversion factors between SI Units and U.S. Customary Units are given in Reference 7. The symbols used in the present report are defined as follows:

$c$	Chord of basic airfoil (flap retracted)
$c'_f$	Local skin friction coefficient, $\frac{\tau}{q_\infty}$
$c_l$	Airfoil section lift coefficient, $\frac{\text{section lift}}{q_\infty c}$
$c_{ps}$	Static pressure coefficient, $\frac{p_s - p_\infty}{q_\infty}$
$c_{pt}$	Total pressure coefficient, $\frac{p_t - p_\infty}{q_\infty}$
$h$	Razor blade thickness/2
$p_s$	Local static pressure
$p_t$	Local total pressure
$p_\infty$	Free stream static pressure
$q_\infty$	Free stream dynamic pressure
RN	Reynolds number based on wing chord
$s$	Curvilinear distance along the airfoil surface

$T$	Turbulence, ratio of peak perturbation velocity to local mean, from hot-film trace
$U$	Velocity at the edge of the boundary layer, non-dimensionalized with respect to free stream velocity
$u$	Local velocity, non-dimensionalized with respect to free stream velocity
$u_e$	Velocity at the outer edge of the confluent boundary layer, non-dimensionalized with respect to free stream velocity
$u_m$	Maximum velocity of the confluent boundary layer, non-dimensionalized with respect to free stream velocity
$u_w$	Wake minimum velocity of the confluent boundary layer, non-dimensionalized with respect to free stream velocity
$u_x$	Component of local velocity in the free stream direction, non-dimensionalized with respect to free stream velocity
$u_\infty$	Free stream velocity
$x_a$	Coordinate along airfoil chord
$x_f$	Coordinate along flap chord
$x_w$	Streamwise coordinate in wake, zero at flap trailing edge
$z$	Coordinate normal to free stream, zero at local surface, or zero at flap trailing edge in the wake
$\alpha$	Angle of attack, degrees
$\Delta p$	Pressure difference between the pressure reading with razor blade in position and the true undisturbed static pressure
$\delta_f$	Flap deflection angle, measured from flap chord line in the retracted position
$\rho$	Density of air
$\nu$	Kinematic viscosity
$\tau$	Shear stress

## APPARATUS AND PROCEDURE

### TESTS

The experimental investigations were carried out in the WSU 213cm x 305cm (7' x 10') low speed wind tunnel fitted with a 213cm x 91.4cm (7' x 3') two-dimensional insert employing a 17% thick GA(W)-1 airfoil section with a .3c Fowler flap (Fig. 2). The basic airfoil section has a chord of 61cm (24") and a span of 91.4cm (36"). Details of the model construction, supporting disks and the surface pressure taps are given in Reference 2. Reynolds number of the test was  $2.2 \times 10^6$  based on the airfoil chord and Mach number was 0.13. Transition was ensured by employing 2.5mm (0.1") wide strips of 80# carborundum grit at .05c on both upper and lower surfaces. Details of the flow fields were investigated on both upper and lower surfaces. Angles of attack for the 40° flap deflection were 2.7°, 7.7° and 12.8°, and those for the flap nested condition were 10.3°, 14.4° and 18.4°. At each angle of attack, about fifteen chordwise survey stations were selected, covering airfoil and flap upper and lower surfaces and the wake. Surveys were also conducted at the slot exit for three typical slot geometries representing narrow, wide and optimum gaps.

### INSTRUMENTATION

Velocities were obtained by employing a five-tube pressure sensing pitch-yaw probe of 3.2mm (.125") diameter (Fig. 3). The details of the construction and operation are given in References 7 and 8. In addition to the five-tube pressure probe, a boundary layer mouse (Fig. 4) consisting of 28 total head tubes of 0.711mm (.028") diameter was employed to obtain total pressure data very near the surface and up to about 22mm (0.96") above the surface.

Hot-film surveys were also conducted to scan the regions of moderate and heavy turbulence employing a 0.05mm (.002") diameter probe with linearizer (Fig. 5).

Local skin friction was measured by the technique outlined by East (Ref. 10), employing commercially available razor blades of 0.094mm (.0037") thickness. Each blade was trimmed to a 3.2mm (.125") square and was positioned at the surface static pressure orifice where the local skin friction was to be evaluated. Details of the razor blade dimensions are given in Figure 6. Unbonded strain gage pressure transducers with a range of  $\pm 17.2$  kilonewtons/m<sup>2</sup> ( $\pm 2.5$ psi) were used for all pressure measurements.

#### METHODS

Surface pressures were obtained through a system of pressure switches and transducers with digital data recorded on punch cards. Flow velocity data was acquired by initially tilting the five-tube probe to align with the local slope of the airfoil surface at the mid-span of the model. The probe was then yawed into the plane of the local flow and all five pressures were recorded on punch cards along with probe position. Total pressure measurements were obtained by aligning the boundary layer mouse in the direction of the local surface. The airfoil and flap combination was inverted while scanning the lower surface flow. Measurements in the wake regions were made with the probe tilted to align with an average downwash within the wake and yawed as required into the local flow.

Hot-film surveys were made with the traversing mechanism employed for the five-tube survey probe. The fixture was suitably modified to hold the hot-film probe and the support gear. Photographs of the velocity fluctuations displayed on the oscilloscope were also recorded.

Local skin friction was measured by positioning the razor blade as shown in Figure 6. This method involves relating the skin friction ( $\tau$ ) to the difference between the pressure recorded by the static hole with the blade in position, and the true undisturbed local static pressure (blade removed). Geometrical limitations such as the ratio of the static pressure orifice diameter to the blade height, bevel angle of the blade, blade width and length, and positioning of the blade with respect to the static pressure hole are discussed in detail by East (Ref. 10). Important dimensions are tabulated in Figure 6, for the present experimental setup.

#### DATA REDUCTION

Local static and total pressures, velocities and flow inclinations were determined from five-tube probe measurements using a computerized data reduction program based upon the probe calibration data given in Reference 9. Pressures and velocities are non-dimensionalized with respect to remote free stream conditions. Velocity profiles were plotted using a computer-controlled digital plotter. All pressure instrumentation employed in the present tests is heavily damped and hence records time-averaged values.

In contrast, the hot-film anemometer instrumentation is capable of measurements up to several thousand Hertz. Typical traces from the hot-film probe were photographically recorded on an oscilloscope and average digital voltmeter readings were recorded manually. The hot-film was calibrated from time to time during the course of the tests to compensate for tunnel temperature variations. Maximum calibration shifts amounted to 6% of free stream velocity.

Local skin friction coefficients were calculated from pressure measurements with the razor blade, utilizing the following equation (Ref. 10).

$$\log_{10} \left( \frac{\tau h^2}{\rho \nu^2} \right) = -0.23 + 0.618 \left[ \log_{10} \left( \frac{\Delta p h^2}{\rho \nu^2} \right) \right] + 0.0165 \left[ \log_{10} \left( \frac{\Delta p h^2}{\rho \nu^2} \right) \right]^2 \quad (1)$$

where  $\tau$  is the local shear stress,  $\Delta p$  is the pressure difference between the surface pressure recorded by the static orifice with the razor blade in position and the undisturbed static pressure,  $h$  is half the razor blade thickness, and  $\nu$  and  $\rho$  are fluid kinematic viscosity and density respectively.

#### PRESENTATION OF RESULTS

The results of the present investigation are presented in the following figures:

<u>Type of data</u>	<u>Instrument</u>	<u>Flap</u>	<u>Gap</u>	<u><math>\alpha</math></u>	<u>Figure</u>
Surface Pressure	--	40°	Optimum (.03c)	2.7°	7(a)
				7.7°	7(b)
				12.8°	7(c)
Velocity profiles	Five-tube probe	40°	Optimum	2.7°	8(a)
				7.7°	8(b)
				12.8°	8(c)
Static pressure contours	Five-tube probe	40°	Optimum	2.7°	9(a)
				7.7°	9(b)
				12.8°	9(c)
Total pressure profiles	Boundary layer mouse	40°	Optimum	2.7°	10(a)
				7.7°	10(b)
				12.8°	10(c)
Slot exit flow	Five-tube probe and Boundary layer mouse	40°	.02 to .04c	2.7°	11(a)
				7.7°	11(b)
				12.8°	11(c)
Total pressure profiles at .10 $x_f/c$	Boundary layer mouse	40°	.02 to .04c	2.7°	12(a)
				7.7°	12(b)
				12.8°	12(c)

<u>Type of data</u>	<u>Instrument</u>	<u>Flap</u>	<u>Gap</u>	<u><math>\alpha</math></u>	<u>Figure</u>
Velocity and pressure profiles on the flap	Five-tube probe	40°	Optimum	2.7°	13(a)
				7.7°	13(b)
				12.8°	13(c)
Total pressure contours	Five-tube probe	40°	Optimum	2.7°	14(a)
				7.7°	14(b)
				12.8°	14(c)
Wake velocity and pressure distributions	Five-tube probe	40°	Optimum	2.7°	15(a)
				7.7°	15(b)
				12.8°	15(c)
Hot-film survey	Hot-film	0°	---	10.3°	16(a)
				14.4°	16(b)
				18.4°	16(c)
Hot-film survey	Hot-film	40°	Optimum	2.7°	17(a)
				12.8°	17(b)
Hot-film surveys on the flap, $0.15 x_f/c$	Hot-film	40°	Optimum	12.8°	18(a)
					18(b)
Hot-film surveys on the flap, $0.25 x_f/c$	Hot-film	40°	Optimum	12.8°	19(a)
					19(b)
Local skin friction distributions	Razor blade	0°	---	0.2°	20(a)
				10.3°	20(b)
				14.4°	20(c)
				18.4°	20(d)
Local skin friction distributions	Razor blade	40°	Optimum	0.2° to 12.8°	21

## DISCUSSION

### Surface Pressure Distributions: (Figure 7)

At pre-stall angles of attack, the pressure distributions indicate separation on the flap upper surface, as evidenced by



a constant pressure region. For the post-stall angle of attack, the flap flow is attached but separation is observed at about .70c on the airfoil upper surface.

Velocity Plots: (Figure 8)

Velocity plots obtained from the five-tube probe measurements show the nature of the flow fields for the airfoil and flap, including boundary layer and wake development. For regions near the surface in the flap cove and at the flap trailing edge station, no data are presented. Measurements made in these regions indicated that either the local dynamic pressure was negative for all yaw angles ( $\pm 180^\circ$ ) or the flow inclination was beyond the calibration limits of the probe ( $> |45^\circ|$ ). This situation is in contrast to earlier research with the GA(W)-1 plain airfoil (Ref. 8) for which satisfactory measurements were obtained at angles of attack up to  $18.4^\circ$ , with separation as far forward as .45c. For the plain airfoil the region of reversal just downstream of the separation point is quite shallow, however. With flap extended, the depth of the reversed flow region grows rapidly and interactions between forward element and flap wakes seem to contribute to flow unsteadiness. At  $12.8^\circ$  angle of attack the separated wake from the airfoil is swept downstream and its unsteadiness prohibits successful velocity measurements at many locations above the flap and in the wake. Several profiles at the post-stall angle (for example, mid-flap chord station and flap trailing edge station), exhibit relatively large changes in velocity between adjacent measurement points.

In Reference 8, data were presented which show that the region of flow reversal in the separated wake of a single-element airfoil terminates a relatively short distance beyond the trailing edge. This point, called the reattachment point, was also characterized by a local maximum static pressure.

In the present tests, the reattachment point evidently occurs between 0 and  $.06 x_w/c$  for the two pre-stall angles of attack. For the post-stall condition, no reattachment is observed for stations as far aft as  $.3 x_w/c$ .

Static Pressure Contours: (Figure 9)

The static pressure contours reflect typical airfoil results, with relatively small regions of highly negative pressure near the upper surface leading edge. The regions of upper surface separation are reflected by isobars nearly parallel to the local surface. The flap cove region shows a local region of increased pressure at all angles of attack. While the research of Reference 8 indicated a local region of increased static pressure near the reattachment point, the present data show no such tendency.

Total Pressure Profiles: (Figure 10)

Total pressure profiles obtained from the boundary layer mouse are useful for determining the extent of the boundary layer and reduced energy wake, since these regions are identified by  $c_{pt}$  values less than unity. At the pre-stall angles of attack, the separation over the rear portion of the flap upper surface and within the airfoil lower surface cove leads to  $c_{pt}$  values lower than local  $c_{ps}$  values. Since the boundary layer mouse presents an unknown interference to reversed flows, no data are presented in the regions of local flow reversal. Although the flap flow is attached at the post-stall angle, the upper surface boundary layer is quite thick as evidenced by the  $c_{pt}$  profiles. In contrast, the flap lower surface exhibits

a very thin layer where  $c_{p_t} < 1.0$  for all three angles of attack. This indicates a very thin boundary layer in this region. This is in accordance with expectations, because of the favorable pressure gradient associated with the flap lower surface flow.

Effects of Slot Gap Variation on Slot Flow: (Figures 11 and 12)

To assess the effects of slot gap variation, limited tests were conducted with narrow (.02c) and wide (.04c) gaps in addition to the optimum (.03c) gap. For the three gap settings, the total pressure profiles at the slot exit for all three angles of attack show center regions of relatively constant  $c_{p_t}$  even though the free-stream value of  $c_{p_t} = 1.0$  is not achieved. The loss in total pressure of 5% to 10% is believed to be caused by upstream flow separation and reattachment in the flap cove. The characteristic shape of the  $c_{p_t}$  profiles suggests that it is reasonable to refer to a "core flow" of constant energy, with sheared flows (wing and flap boundary layers) above and below the core. With the narrow gap, the core is essentially non-existent at the  $0.10 x_f/c$  location for all three angles. With the wide gap a substantial core is provided at  $0.10 x_f/c$  at the two pre-stall angles, but the core is displaced upward compared to the optimum gap case, indicating a tendency for boundary layer thickening on the flap. At the post-stall angle, the wide gap data show that the flap flow has reversed, indicating massive flap separation.

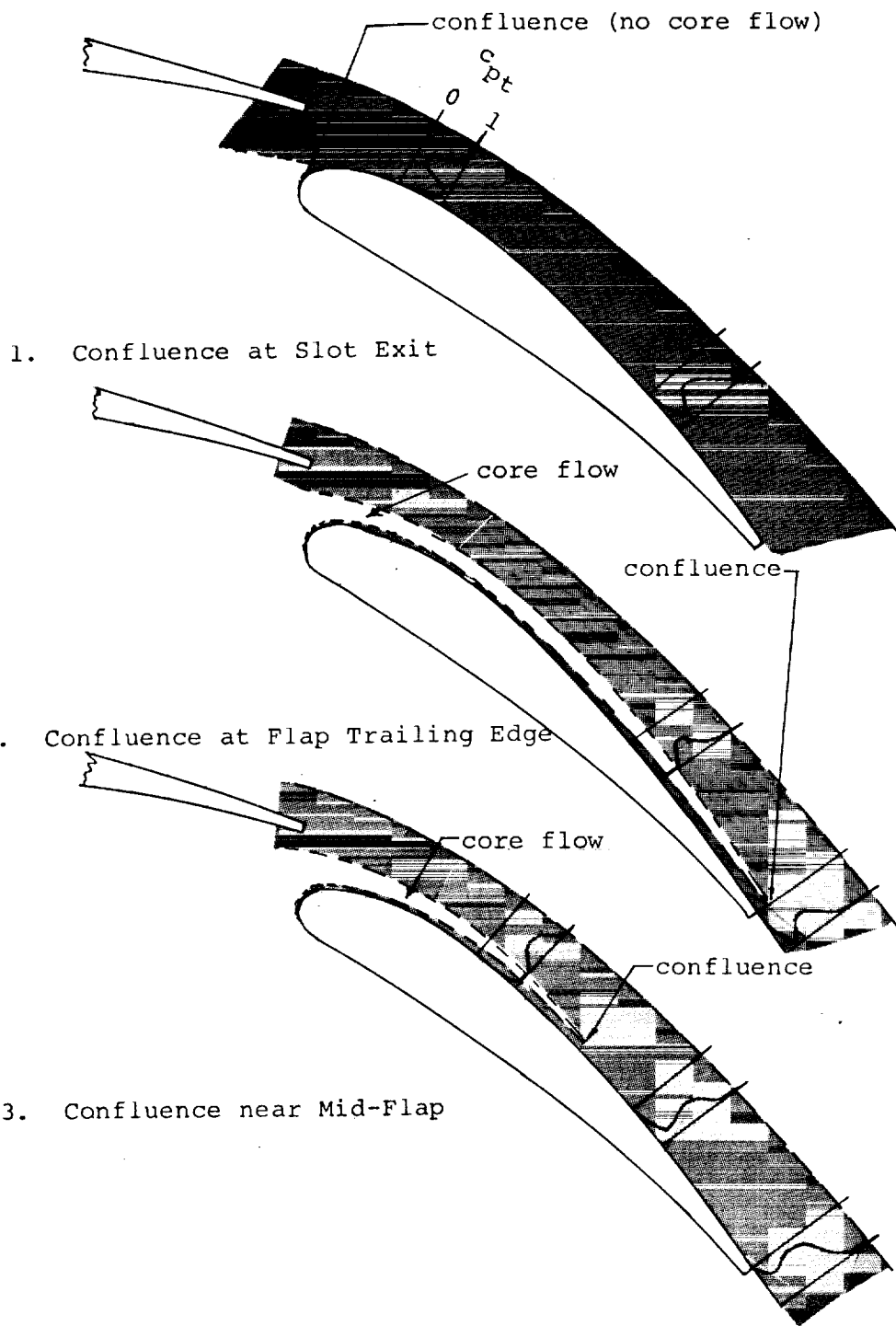
Flow Development on the Flap for Optimum Gap: (Figure 13)

Detailed measurements of total pressure, static pressure and velocity were made at several downstream stations on the

flap for the optimum gap case. These data show that the core flow vanishes at near mid-flap ( $.15 x_f/c$ ) for the pre-stall angles. At the post-stall angle the core vanishes ahead of the  $.075 x_f/c$  location.

Several authors have discussed criteria for an optimum flap slot. According to Foster, et al, (Ref. 3), the criteria for the optimum gap is that the two boundary layers (on the flap upper surface and the lower surface of the airfoil) are just separated by a potential core at the slot exit (Sketch A1). On the other hand, Ljungström (Ref. 4) discusses the necessity for achieving "minimum interaction" between wing wake and flap boundary layer. This would seem to imply the existence of a potential core as far aft as the flap trailing edge. Smith (Ref. 5) suggests that an optimum design will permit "dumping" the forward element wake such that it will have minimum influence on the flap flow. This would also imply the existence of a potential core extending at least as far aft as the flap trailing edge (Sketch A2).

The present data for an optimum slot show that a core flow of finite thickness is present at the slot exit and that this core vanishes as the flap and wing boundary layers merge near the mid-flap-chord location (Sketch A3). Thus it appears that Foster's criteria is in error, and that in fact a finite core must be retained at the slot exit. The present data seem to indicate that confluence of flap and wing vorticity layers can occur forward of the flap trailing edge without disrupting the entire flow. Thus the optimum situation would seem to be a slot which provides a finite core flow at the slot exit, but it is not necessary that the core persist as far aft as the flap trailing edge.



Sketch A - Possible locations of confluence point for optimum flap slot.

Theoretical Analysis of Slot Flow:

The mathematical model developed by Goradia, et al, for confluent boundary layer analysis of multi-element airfoils (Ref. 1 and Sketch B), contains several restrictions which were imposed because of data limitations or computational instabilities. Some of the restrictions are:

1. Non-dimensional maximum velocity,  $u_m/u_e \geq 1$ . This was based on the best experimental data available.

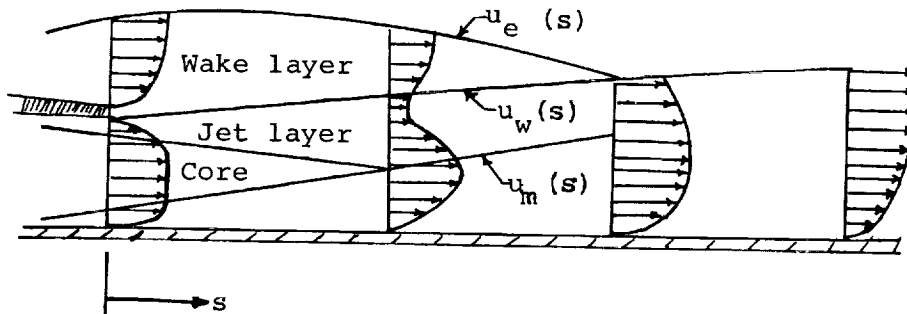
2. Streamwise gradient of non-dimensional maximum velocity,

$$-0.8 \leq \left( d\left(\frac{u_m}{u_e}\right) / d\left(\frac{s}{c}\right) \right) \leq 0.8.$$

3. Streamwise gradient of non-dimensional wake velocity,

$$-0.8 \leq \left( d\left(\frac{u_w}{u_e}\right) / d\left(\frac{s}{c}\right) \right) \leq 0.8.$$

Restrictions 2 and 3 were imposed to insure stability of computations.



Sketch B: Confluent Boundary Layer Model (Ref. 1).

Computer studies using the method of Reference 1 were conducted as part of the present research for the 40° flap with optimum gap. These studies yielded messages indicating errors in the confluent boundary layer computations,

and the computer results were therefore invalid. In order to determine whether the program limitations on maximum core velocity ratio and on wake and maximum velocity gradients outlined above are realistic, determinations of these values have been carried out from experimental measurements near the slot exit. The experimental values are given in Table 1:

Table 1: Experimental Velocity Ratios and Gradients -  
40° Flap, Optimum Gap

$\alpha$	$x_f/c$	$u_m$	$u_w$	$u_e$	$u_m/u_e$	$u_w/u_e$	$\frac{d(u_m/u_e)}{d(s/c)}$	$\frac{d(u_w/u_e)}{d(s/c)}$
2.7°	.075	1.315	1.07	1.387	<u>0.9481</u>	0.7714	-1.1363	-.9151
	.15	1.058	0.862	1.26	<u>0.8397</u>	0.6841		
7.7°	.075	1.193	0.874	1.337	<u>0.8923</u>	0.6537	-1.0996	-.9675
	.15	1.000	0.713	1.27	<u>0.7874</u>	0.5614		

Note: 1.  $\Delta x/c$  of .075 corresponds to  $\Delta s/c$  of .0954 at this location.  
2. Gradients are computed using  $\Delta s/c$ .

Comparisons of the experimental values with computer program limits are given in Table 2:

Table 2: Confluent Boundary Layer Parameters -  
Theory and Experiment

Parameter Definition:	Symbol	Theoretical Limits	Reason for Limit	Experimental Values
Non-dimensional maximum velocity	$\frac{u_m}{u_e}$	$\geq 1.0$	Lack of Data	0.79 to 0.95
Streamwise gradient of non-dimensional maximum velocity	$\frac{d(u_m/u_e)}{d(s/c)}$	-0.8 to 0.8	Instability	-1.10 to -1.14
Streamwise gradient of non-dimensional wake-velocity	$\frac{d(u_w/u_e)}{d(s/c)}$	-0.8 to 0.8	Instability	-0.92 to -0.97

These data show that the computer program limitations are exceeded for all three parameters at pre-stall angles of attack with optimum flap gap geometry.

Total Pressure Contours: (Figure 14)

At the pre-stall angles, these data show that the viscous wake ( $c_{pt} < 1$ ) extends to approximately .15c above the flap and .03c below the flap. At the post-stall angle the wake region is much wider, and flows essentially straight aft from the airfoil trailing edge. The lower limit of the wake region was not reached for this case, due to instrumentation travel limits, but it appears that the wake extends more than .15c below the trailing edge.

Velocity and Pressure Distributions in the Wake for Optimum Gap:  
(Figure 15)

Total pressure, static pressure and velocity profiles for a vertical range of about  $-.10c$  to  $.25c$  at 4 chordwise stations within the wake show the progressive growth of the wake width in the longitudinal direction. A rather gentle vertical pressure gradient can also be seen.

In general, the profiles are very smooth at pre-stall angles of attack and become irregular at the post-stall angles of attack evidently as a result of intense turbulent fluctuations in the vertical and longitudinal directions. Satisfactory post-stall measurements could not be made even at  $.30 x_w/c$ .

Hot-Film Surveys: (Figures 16 and 17)

Hot-film survey information is presented as maps showing regions with various degrees of turbulence defined by typical oscilloscope traces. Since a single-channel hot-film anemometer is not capable of providing flow direction information, interpretation of the hot-film data for flow reversal is done in the following manner: the flow is considered to be reversing whenever the trace indicates zero on the oscilloscope. The present data (Fig. 16) indicate that the regions of flow reversal extend further



downstream than previous results obtained with pressure-type velocity probes (Ref. 8). At the edges of reversal zones, the flow is intermittently reversing (less than 50% of the time), according to the interpretation used for these data, whereas a pressure-type velocity probe would probably not sense intermittent reversals, because of the inherent instrument damping.

Hot-film surveys conducted with 40° flap indicate a reattachment point (end of flow reversal region) at about  $.2 x_w/c$  for  $\alpha = 2.7^\circ$  and beyond  $.5 x_w/c$  for the post-stall angle. The apparent discrepancies in extent of reversed flow regions between pressure-probes and hot-film probes are attributed to the different damping characteristics of the instruments: the hot-film is highly responsive and senses intermittent reversals while the pressure probes sense only time-averaged reversal.

The hot-film surveys show smooth (relatively low turbulence) flow within the slot exit at all angles of attack, indicating a near optimum slot.

#### Discussion of Problems Associated with Measurements in the Vicinity of Separated Regions:

It is seen from Figure 8 that there are regions in the velocity profiles on the flap and in the wake at the post-stall angle of attack where satisfactory five-tube probe measurements were not obtained. This figure also shows a few profiles which exhibit abrupt changes in the magnitude of velocity between adjacent points in the vicinity of the flap surface. Total pressure measurements obtained from the five-tube probe and the boundary layer mouse did not agree at these locations. At the pre-stall angles of attack the five-tube velocity data agree well with the hot-film data (Figs. 8 and 17). The data in Figure 12(c) which was measured with the boundary layer mouse show a very narrow core flow ( $c_{pt} \approx 1$ ) at  $0.10 x_f/c$  for the optimum gap, whereas the five-tube

probe data (Fig. 13(c)) show no core at all at  $0.075 x_f/c$ . The reason for these inconsistencies in the pressure data remained a mystery until the hot-film measurements were made.

Manual observations of the hot-film anemometer signal on the oscilloscope indicated two distinct mean velocity levels occurring intermittently. The velocity traces in Figure 18 illustrate this phenomenon. In this figure, two traces were recorded at different times. By recording a number of sample traces at a given location it was possible to obtain two consecutive traces which contained the high- and low- velocity levels. On several occasions (Figs. 18(a) and 19(a)), single traces were obtained showing the abrupt change from one velocity magnitude to the other. These observations explain the apparent discontinuities observed in the velocity profiles obtained with the pressure probes. Evidently the two velocity levels observed with the pressure probes are samples from a flow which is characterized by two distinct modes, with large changes in velocity occurring as the flow shifts from one mode to the second. A dramatic change in flow character is seen at the highest station shown in Figures 18 and 19, as the probe moves out of the highly turbulent wake flow into an essentially undisturbed free-stream. The surface pressure data (Fig. 7(c)) and the flow visualization data (Ref. 1) indicate that the flap flow is attached at the post-stall angle of attack ( $\alpha = 12.8^\circ$ ), but the hot-film data show (Fig. 17(b)) intermittent reversal near  $.10 x_f/c$  on the flap. Thus the flow over the flap aft of this station is characterized by low velocity and high velocity modes occurring intermittently, combined with high intensity turbulence. It is therefore clear that the apparent discrepancies in data obtained from the pressure-type instruments are due to the large changes in velocity as the flow changes from the first mode to the second. It should also be noted that the regions of turbulent fluctuations in the flow fields of the multi-

element configurations at post-stall angles of attack are much larger than those of the single-element configurations (Fig. 16 and Ref. 8).

Skin Friction Distributions: (Figures 20 and 21)

For the basic airfoil at a low angle of attack ( $\alpha = 0.2^\circ$ ) the flow is fully attached and the theoretical skin friction distribution calculated by the method of Reference 1 compares very favorably with the experimental results. At a moderate angle of attack of  $10.3^\circ$  (about  $6^\circ$  below stall), flow separation was observed at  $.80 x_a/c$  (Ref. 8), whereas the theory predicts flow separation at  $0.95 x_a/c$  (zero skin friction). The agreement between theory and experiment at this angle of attack is very reasonable in the attached flow regions (Figure 20(b)). A gradual loss in the accuracy of theoretical data occurs with increasing angle of attack as shown by the distribution for an angle of attack of  $14.4^\circ$  ( $2^\circ$  below stall). At the post-stall angle of attack of  $18.4^\circ$ , separation occurs at  $.45 x_a/c$  and the agreement between experiment and theory is poor. It is recognized that the present theoretical model is limited to attached flows so good agreement is not expected when separation is present. These results have been included in order to illustrate the extent of usefulness of the present theory.

Several attempts were made to obtain skin friction data aft of the separation point by positioning the blade in the direction of reversed flow. Measurements made in these regions were inconclusive; that is, a pressure decrease was indicated for both forward and reversed orientations of the razor blade.

Experimental skin friction data for the case of  $40^\circ$  flap deflection with the optimum gap are shown in Figure 21. Theoretical results are not available for this case because of computer program limitations discussed earlier. It is interesting to note that it was possible to obtain measurements for  $10.3^\circ$

angle of attack which corresponds to the maximum lift coefficient. Experimental results for angles of attack up to  $10.3^\circ$  generally show trends similar to the single element airfoil results, except for the slight increasing trend in the skin friction between the  $.20$  and  $.60 x_a/c$  stations. The reasons for this trend are not known. At the pre-stall angles of attack, separation is present on the flap and therefore satisfactory skin friction measurements were not obtained beyond  $.10 x_f/c$ .

### CONCLUSIONS

1. Experimental velocity profiles, static and total pressure distributions and turbulence measurements have been obtained for the GA(W)-1 airfoil with a  $0.30c$  Fowler flap deflected  $40^\circ$  at typical pre- and post-stall angle of attack conditions for a Mach number of  $0.13$  and a Reynolds number of  $2.2 \times 10^6$ .

2. Measurement difficulties were encountered in the regions of flow reversal. Hot-film surveys in regions of high turbulence were useful in determining the limitations of pressure-type velocity instrumentation.

3. For flap deflected with optimum slot gap, the present tests reveal that the airfoil lower surface boundary layer and the flap upper surface boundary layer at the slot exit are separated by a finite width core flow of constant energy. This core vanishes near the mid-flap chord station.

4. Local skin friction measurements were obtained up to the separation point for the basic and flapped configurations. The measurements on the basic airfoil agree well with theory for angles of attack below stall.

### RECOMMENDATIONS

1. Pre- and post-stall characteristics of the flow field should be investigated for intermediate settings of the Fowler flap (less than  $40^\circ$  deflection).

2. Flow field surveys should be conducted for airfoils having different pressure distributions, such as the thicker (> 20%) GA-airfoils.

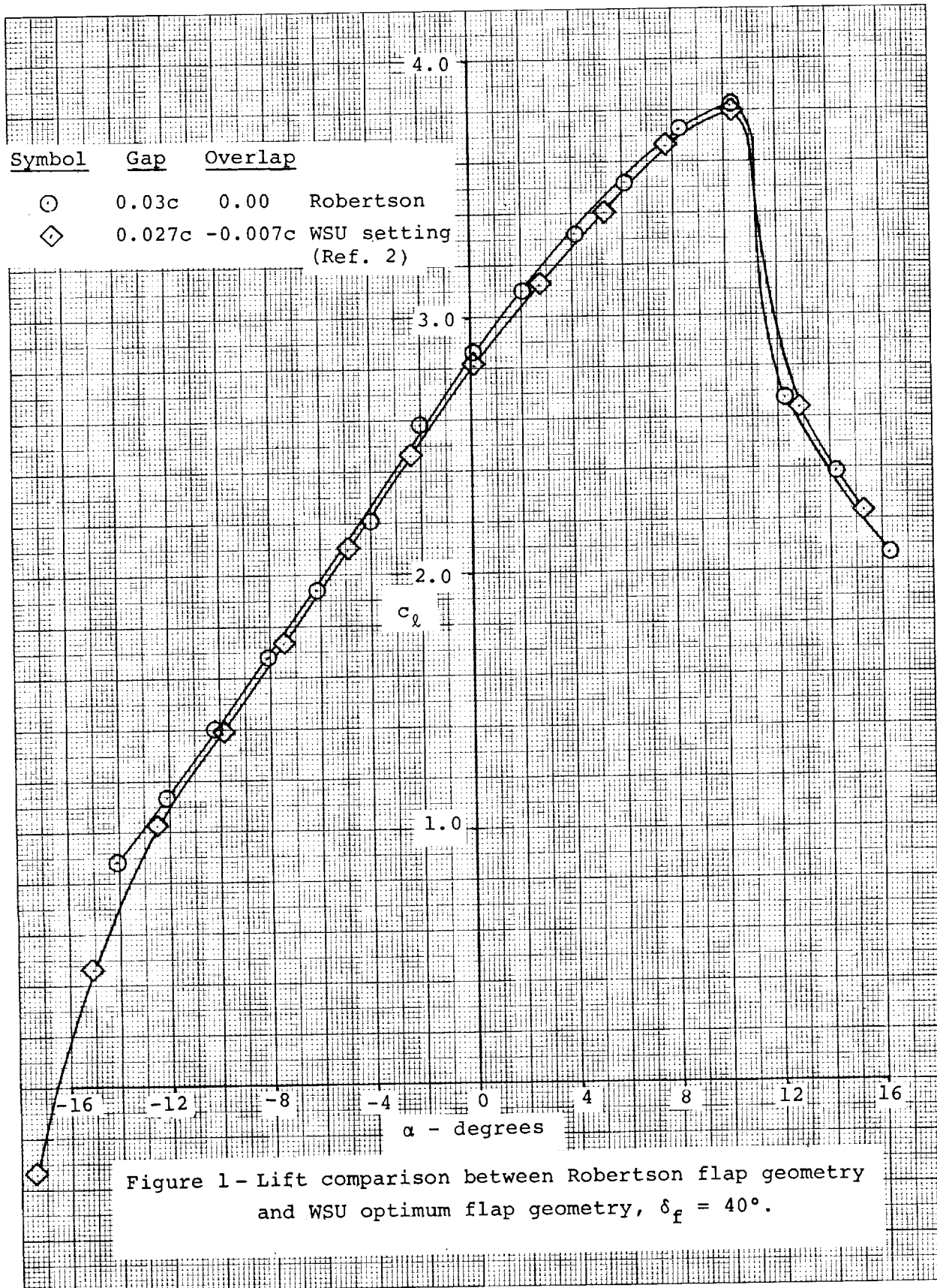
3. Cross film or split film sensors should be employed to measure the velocities and flow inclinations in the highly turbulent regions instead of the pressure type probes. In order to determine static pressure in the highly turbulent wake, special "dime" or "disc" type static pressure probes should be employed with miniature pressure transducers.

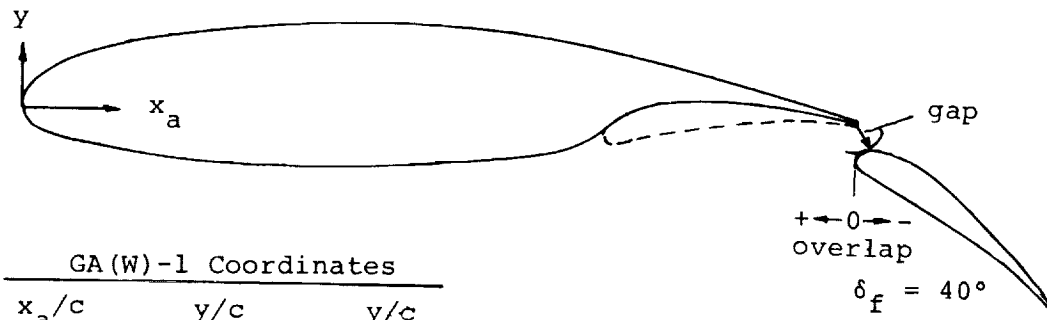
4. In order to understand the basic character of the regions of large scale turbulence, spectral analysis of hot-film data should be carried out.

Department of Aeronautical Engineering  
Wichita State University  
Wichita, Kansas 67208  
October 1976

## REFERENCES

1. Stevens, W.A., Goradia, S.H., and Braden, J.A.: Mathematical Model for Two-Dimensional Multi-Component Airfoils in Viscous Flow. NASA CR-1843, 1971.
2. Wentz, W.H., Jr., and Seetharam, H.C.: Development of a Fowler Flap System for a High Performance General Aviation Airfoil. NASA CR-2443, 1974.
3. Foster, D.N., Irwin, H.P.A.H., and Williams, B.R.: The Two-Dimensional Flow Around a Slotted Flap. British R & M No. 3681, 1971.
4. Ljungström, B.L.G.: Experimental High Lift Optimization of Multiple Element Airfoils. AGARD CP-143, Conference Proceedings on V/STOL Aerodynamics, pp. 13-1 to 13-16, 1974.
5. Smith, A.M.O.: Aerodynamics of High-Lift Airfoil Systems. AGARD CP-102, pp. 10-1 to 10-24, 1972.
6. Holmes, B.J.: Flight Evaluation of an Advanced Technology Light Twin-Engine Airplane. NASA CR-2832, 1977.
7. Mechtley, E.A.: The International System of Units--Physical Constants and Conversion Factors (Revised). NASA SP-7012, 1969.
8. Seetharam, H.C., and Wentz, W.H., Jr.: Experimental Studies of Flow Separation and Stalling on a Two-Dimensional Airfoil at Low Speeds. NASA CR-2560, 1975.
9. Seetharam, H.C., Wentz, W.H., Jr., and Walker, J.K.: Measurement of Post-Separated Flow Fields on Airfoils, AIAA Paper No. 75-1426, 1975.
11. East, L.F.: Measurement of Skin Friction at Low Subsonic Speeds by the Razor-Blade Technique. British R & M No. 3525, 1968.





GA(W)-1 Coordinates		
$x_a/c$	$y/c$	$y/c$
	Upper Surface	Lower Surface
.0000	.00000	.00000
.0020	.01300	-.00930
.0050	.02040	-.01380
.0125	.03070	-.02050
.0250	.04170	-.02690
.0375	.04965	-.03190
.0500	.05589	-.03580
.0750	.06551	-.04210
.1000	.07300	-.04700
.1250	.07900	-.05100
.1500	.08400	-.05430
.1750	.08840	-.05700
.2000	.09200	-.05930
.2500	.09770	-.06270
.3000	.10160	-.06450
.3500	.10400	-.06520
.4000	.10491	-.06490
.4500	.10445	-.06350
.5000	.10258	-.06100
.5500	.09910	-.05700
.5750	.09668	-.05400
.6000	.09371	-.05080
.6250	.09006	-.04690
.6500	.08599	-.04280
.6750	.08136	-.03840
.7000	.07634	-.03400
.7250	.07092	-.02940
.7500	.06513	-.02490
.7750	.05907	-.02040
.8000	.05286	-.01600
.8250	.04646	-.01200
.8500	.03988	-.00860
.8750	.03315	-.00580
.9000	.02639	-.00360
.9250	.01961	-.00250
.9500	.01287	-.00260
.9750	.00609	-.00400
1.0000	-.00070	-.00800

.30c Fowler Flap Coordinates		
$x_f/c$	$y/c$	$y/c$
	Upper Surface	Lower Surface
.0000	-.01920	-.01920
.0250	.00250	-.02940
.0500	.01100	-.02490
.0750	.01630	-.02040
.1000	.01900	-.01600
.1250	.01950	-.01200
.1500	.01820	-.00860
.1750	.01670	-.00580
.2000	.01330	-.00360
.2250	.00950	-.00250
.2500	.00530	-.00260
.2750	.00100	-.00400
.3000	-.00435	-.00800

Figure 2 - Coordinates of GA(W)-1 Airfoil and .30c Fowler Flap



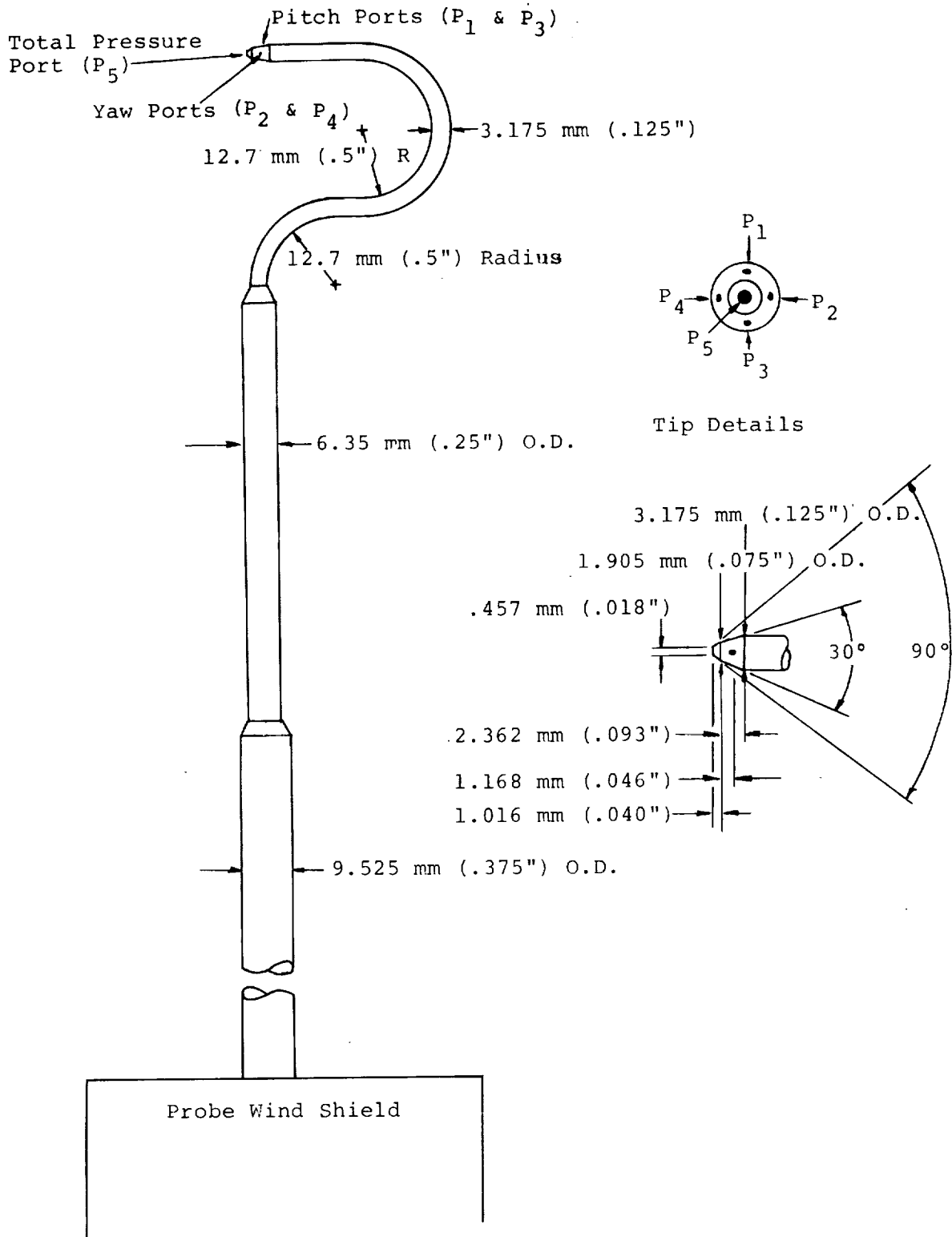


Figure 3 - Five-Tube Probe.

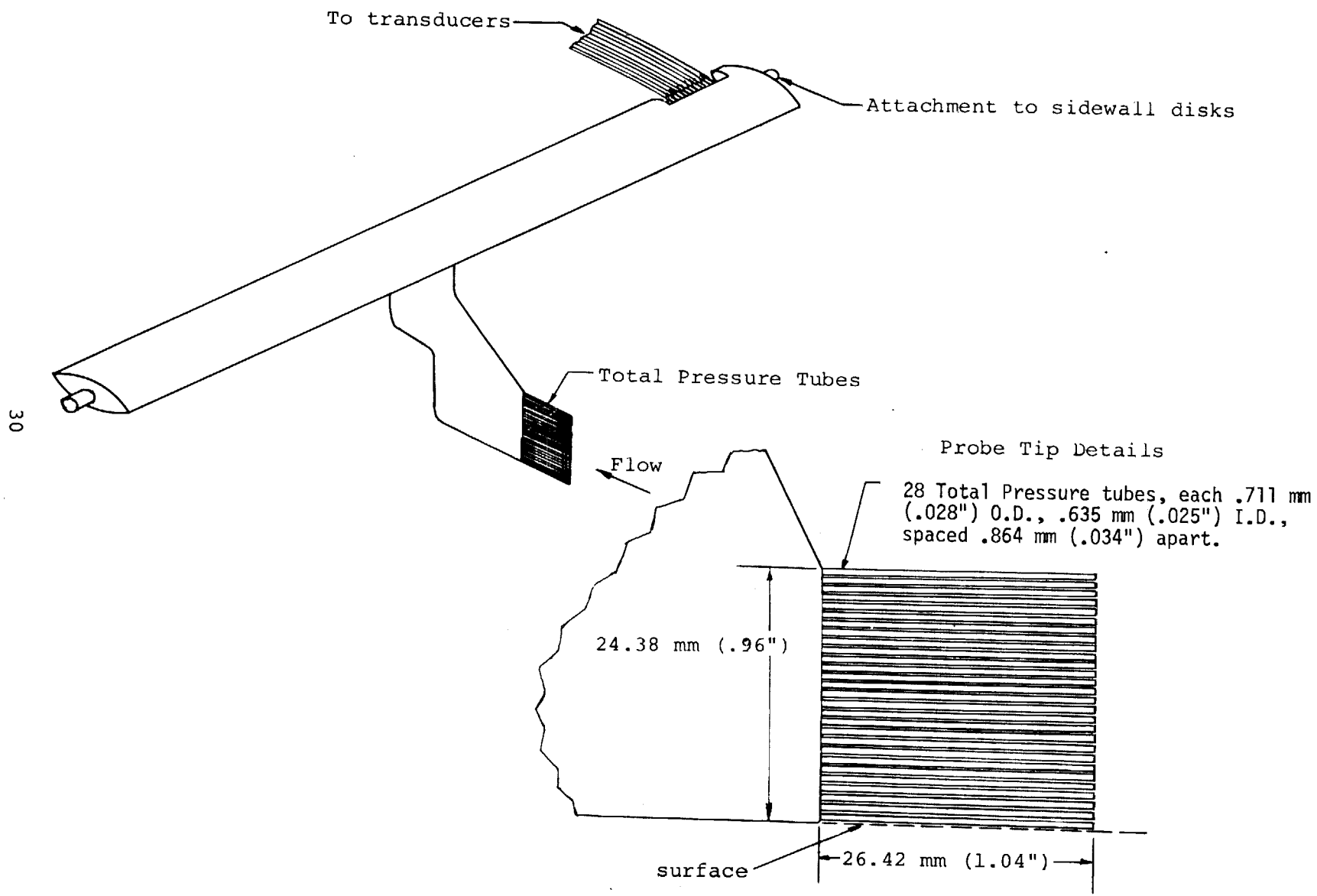
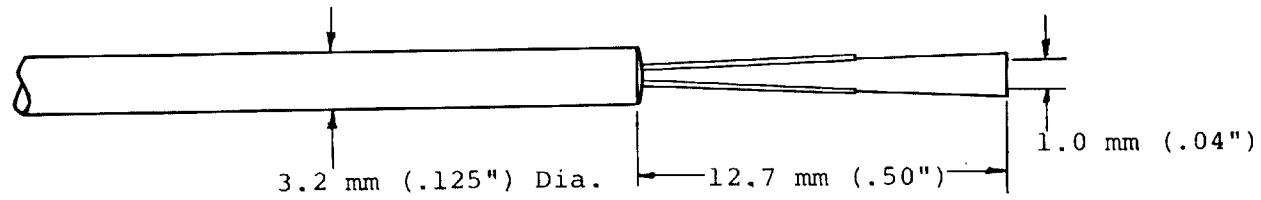
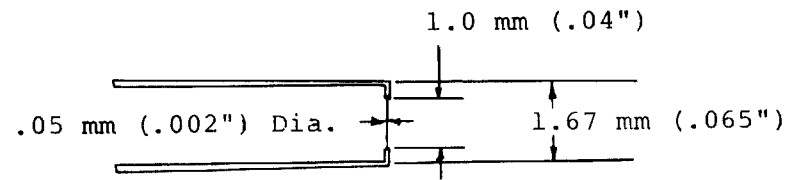


Figure 4 - Boundary Layer Mouse.

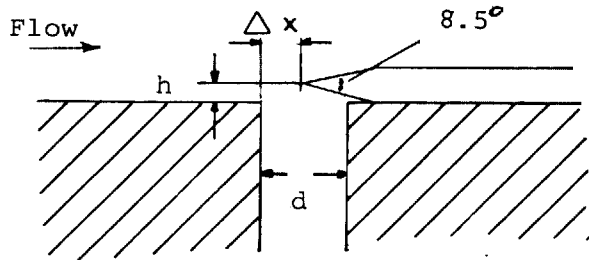


31



Tip Detail

Figure 5 - Hot Film Probe.

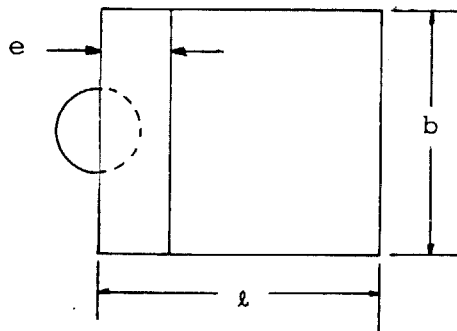


Surface Static Pressure Tap

Dimensions

d	.762 mm (.030")
e	.635 mm (.025")
h	.047 mm (.00185")
ℓ	3.175 mm (.125")
b	3.175 mm (.125")
d/h	16.2
b/h	67.6

32



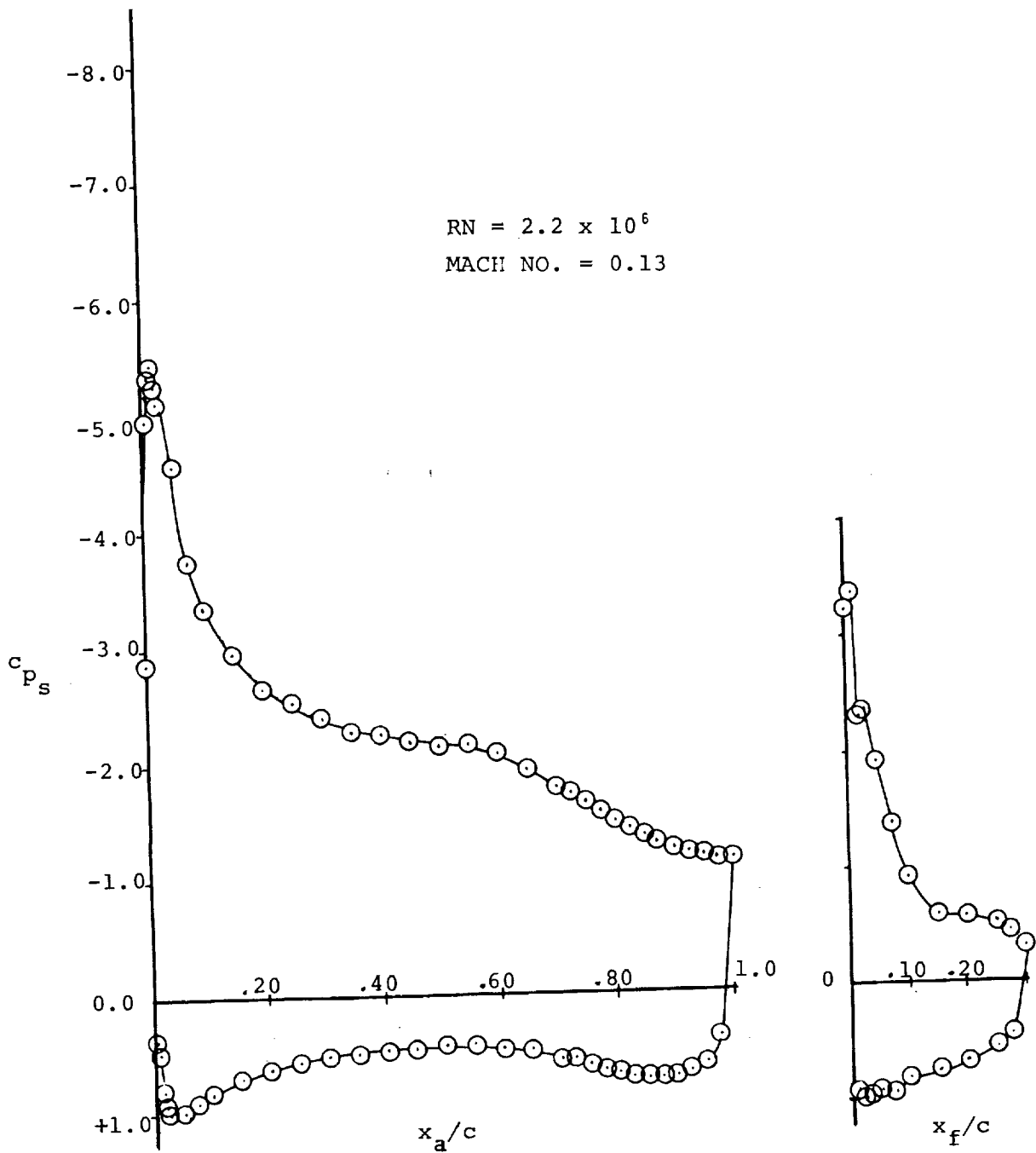
Criteria from Ref. 10:  $\frac{d}{h} > 6$

$$\frac{b}{h} > 36$$

$$\frac{\ell}{b} = 1$$

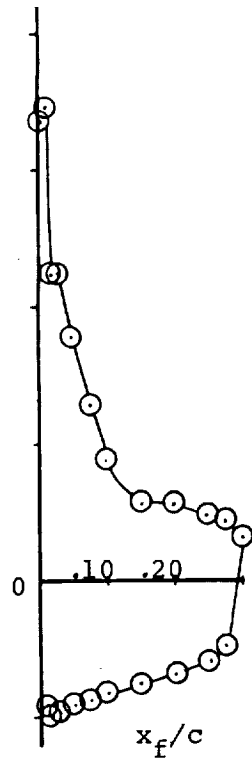
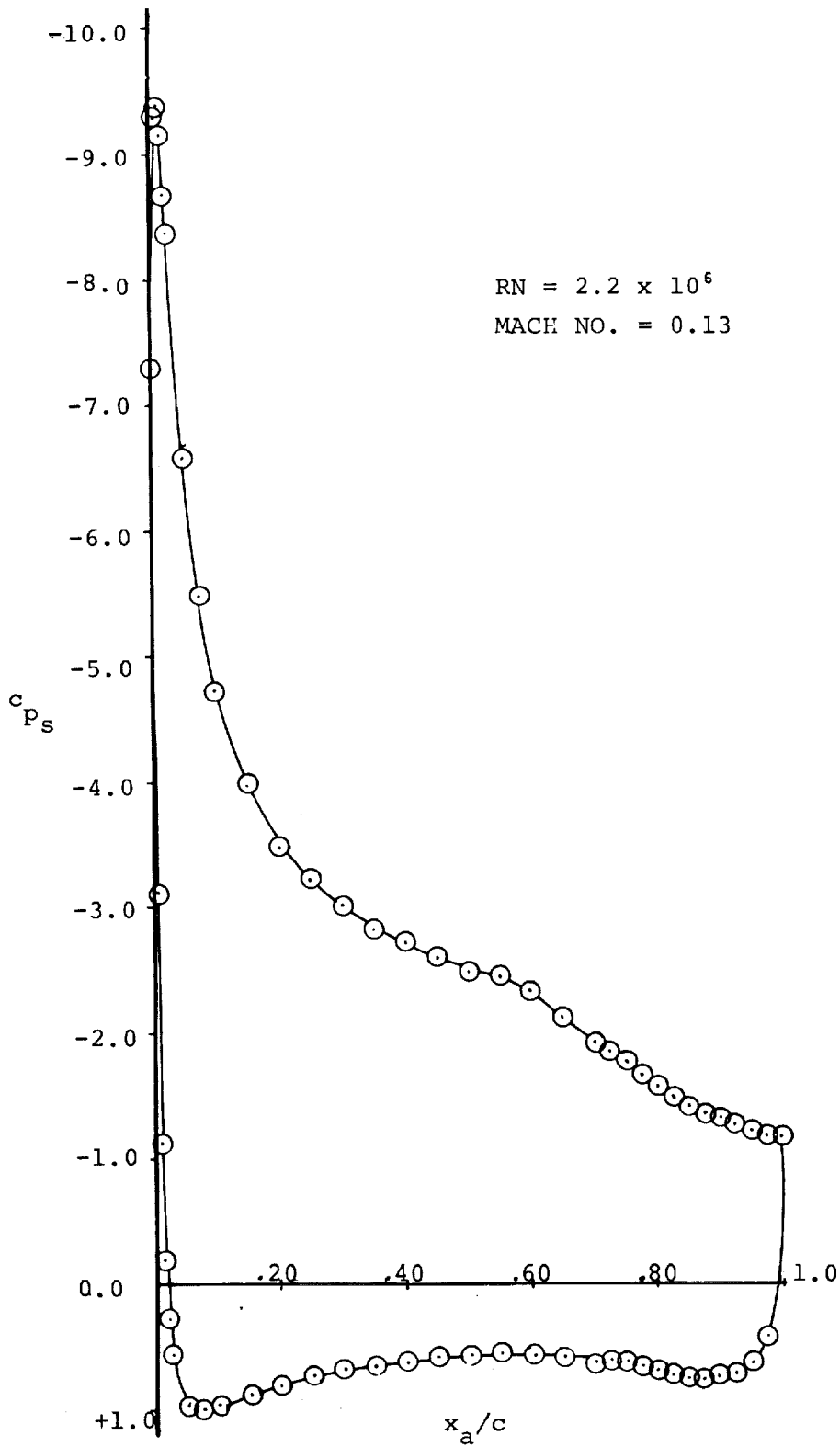
$$\Delta x = 0$$

Figure 6 - Razor Blade Technique: Details of Dimensions and Positioning.

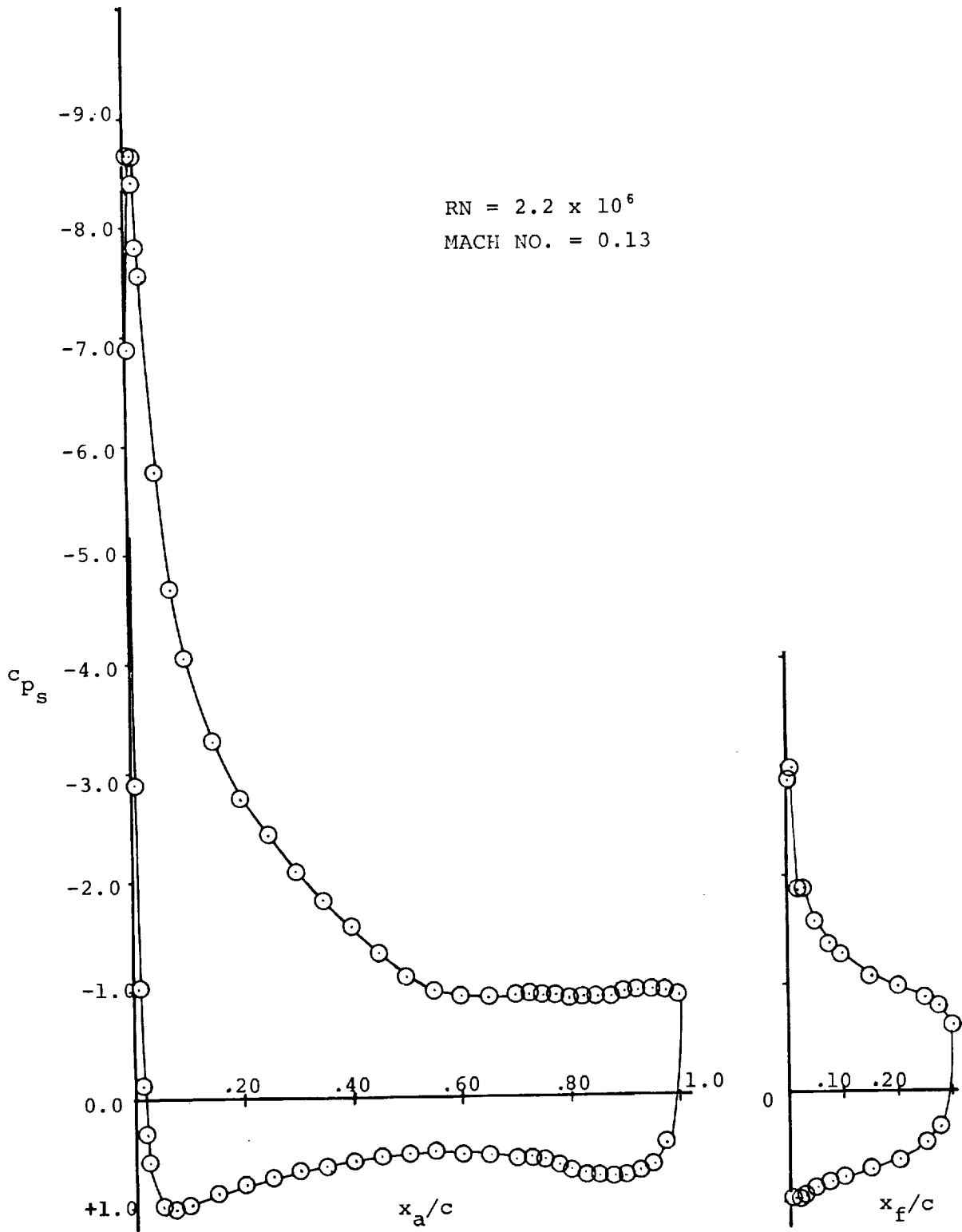


(a)  $\alpha = 2.7^\circ$

Figure 7 - Surface Pressure Distribution.  $\delta_f = 40^\circ$ , Optimum gap.



(b)  $\alpha = 7.7^\circ$   
 Figure 7 - Continued.



(c)  $\alpha = 12.8^\circ$

Figure 7 - Concluded.

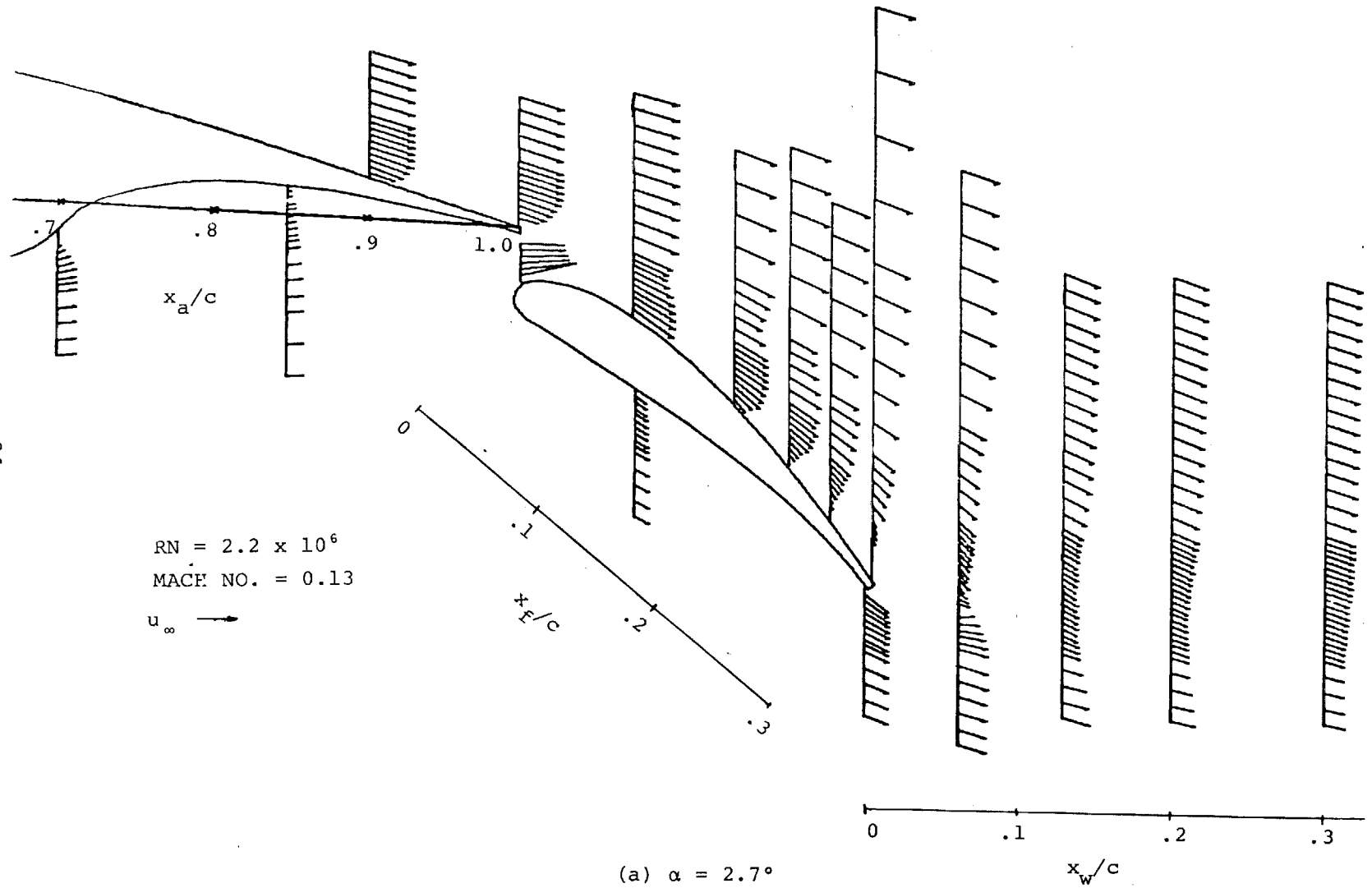
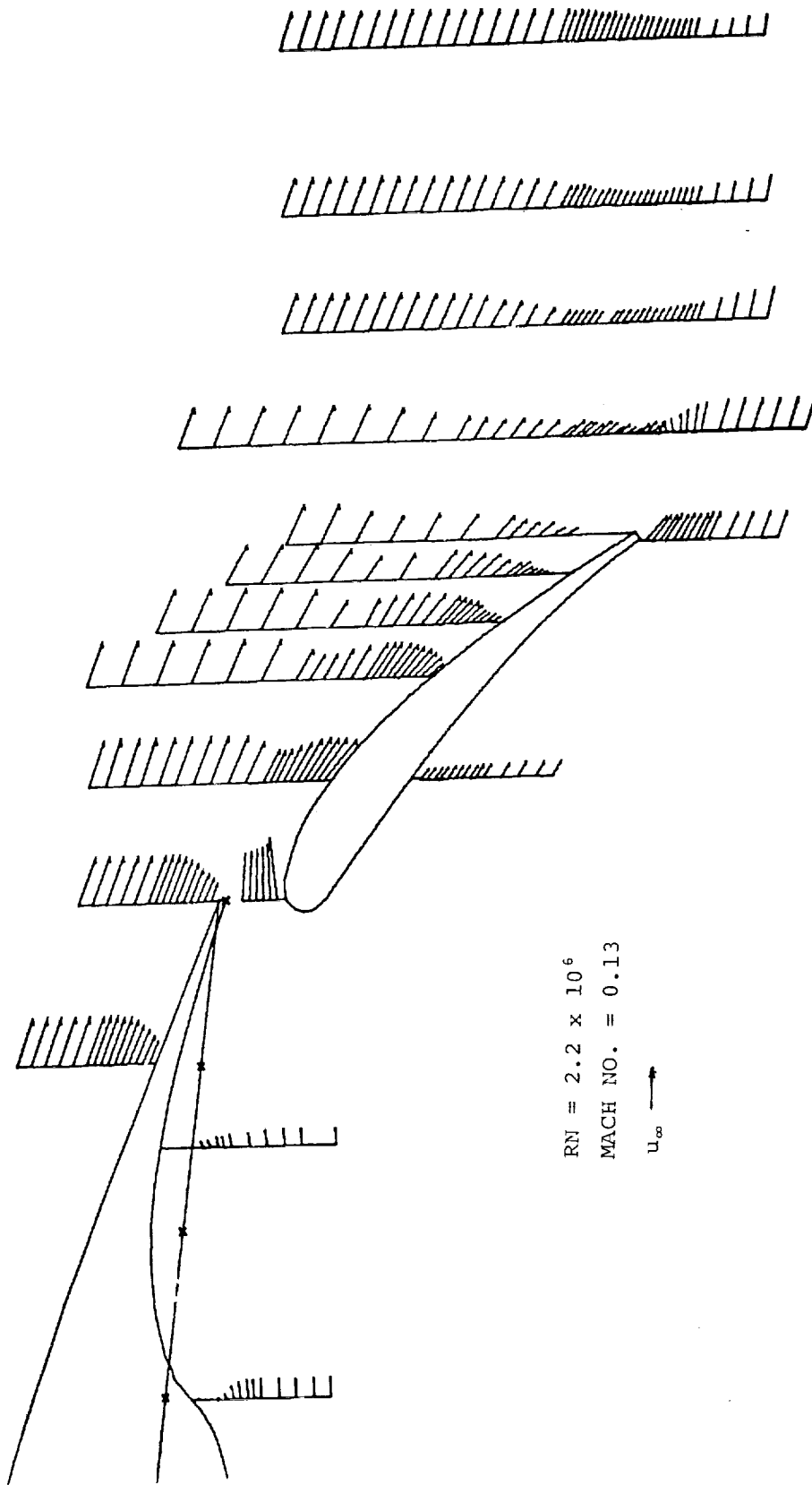


Figure 8 - Experimental Velocity Profiles.  $\delta_f = 40^\circ$ , Optimum gap.





(b)  $\alpha = 7.7^\circ$

Figure 8 - Continued.

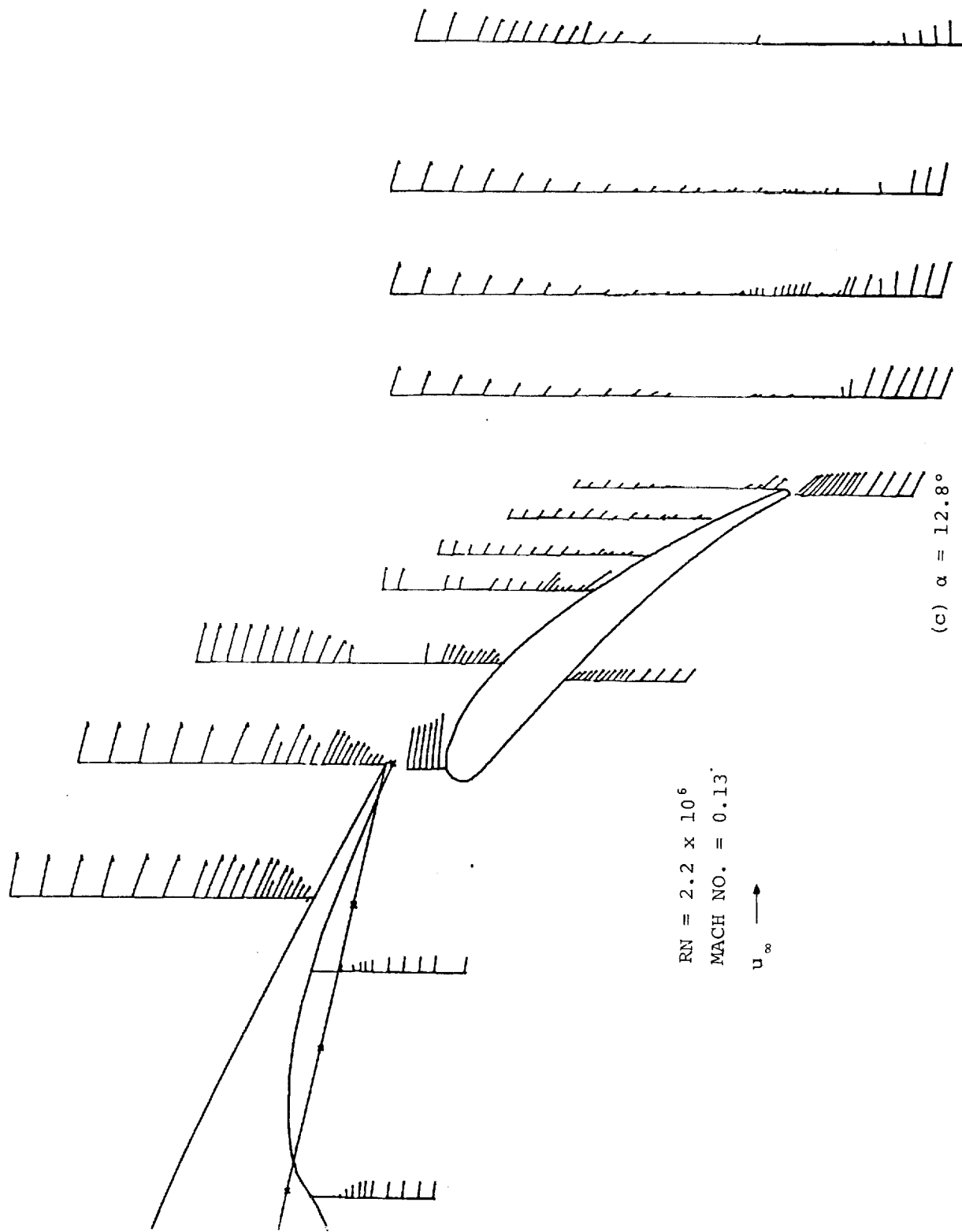
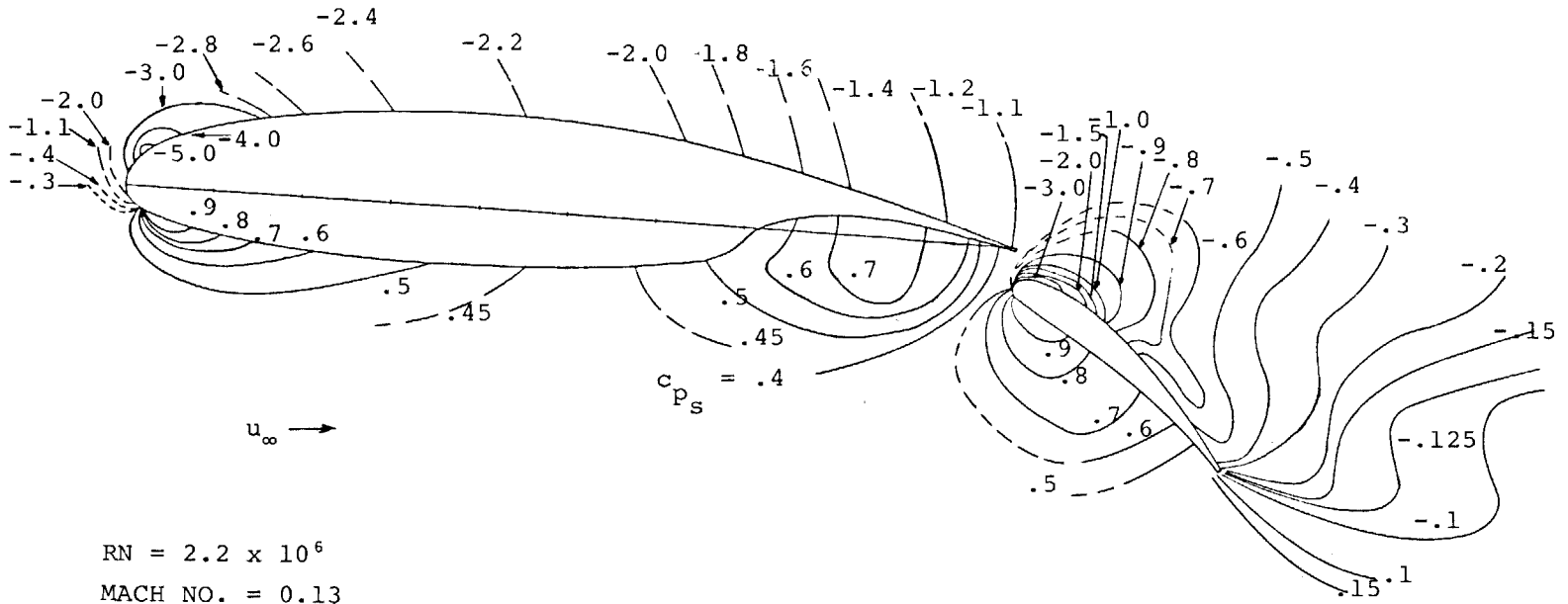
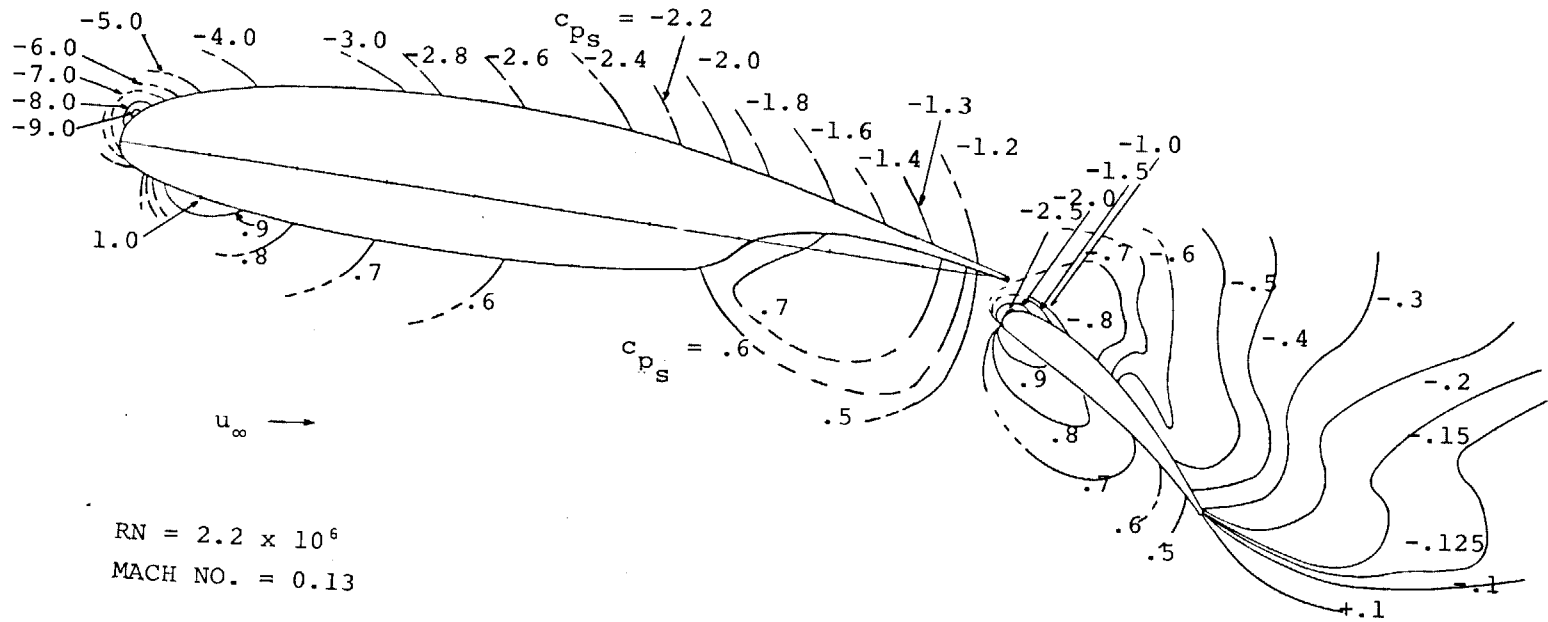


Figure 8 - Concluded.



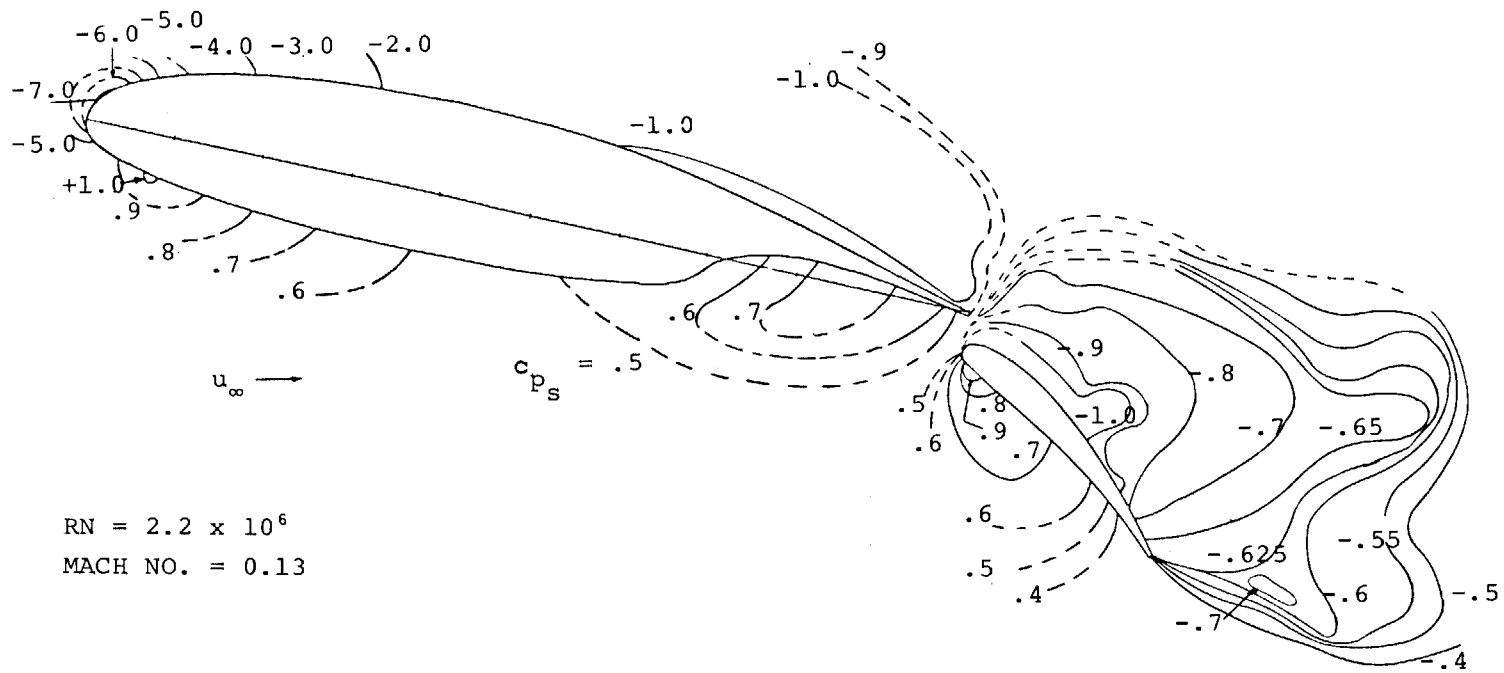
$RN = 2.2 \times 10^6$   
 $MACH NO. = 0.13$

(a)  $\alpha = 2.7^\circ$   
Figure 9 - Static Pressure Contours.  $\delta_f = 40^\circ$ , Optimum gap.



(b)  $\alpha = 7.7^\circ$

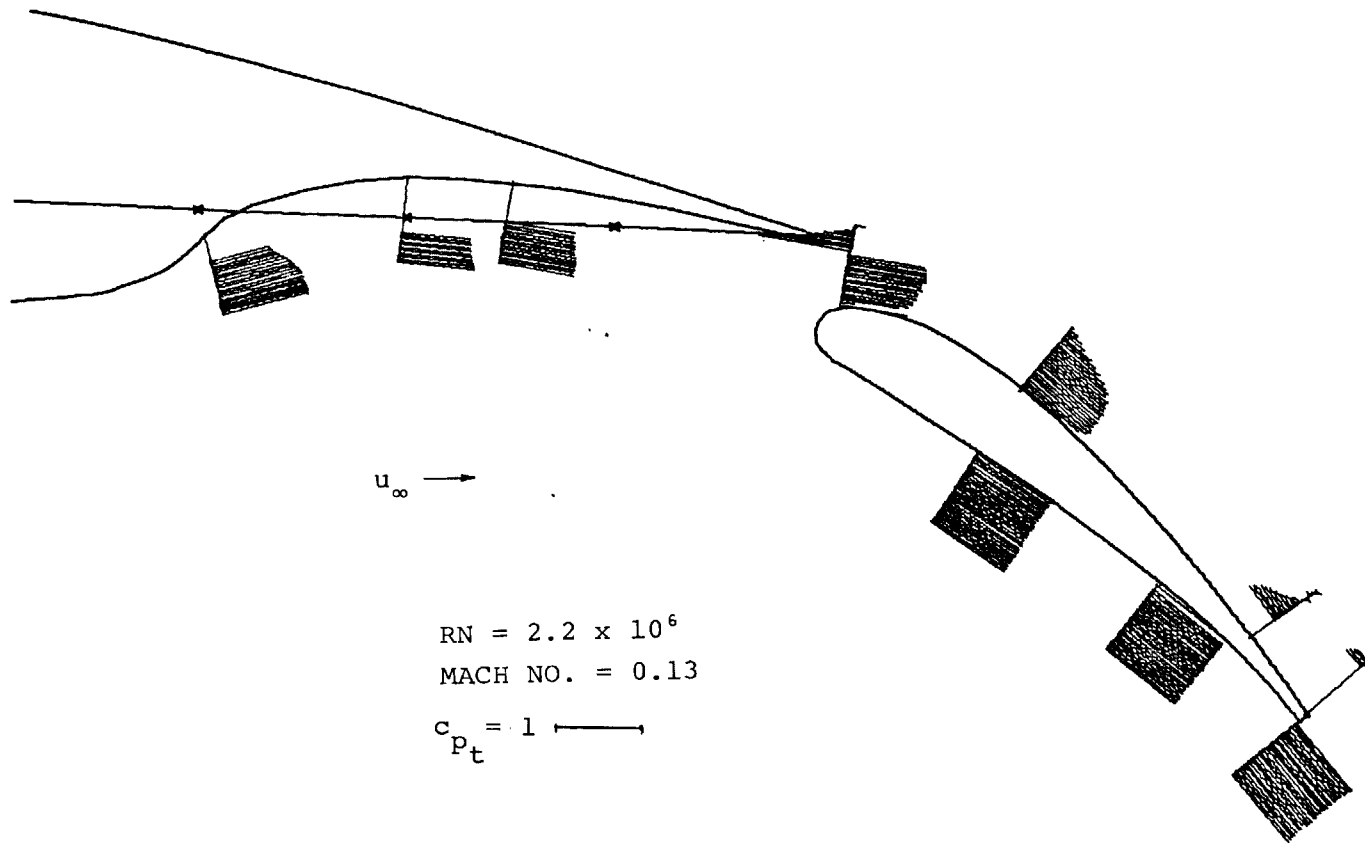
Figure 9 - Continued.



$RN = 2.2 \times 10^6$   
 MACH NO. = 0.13

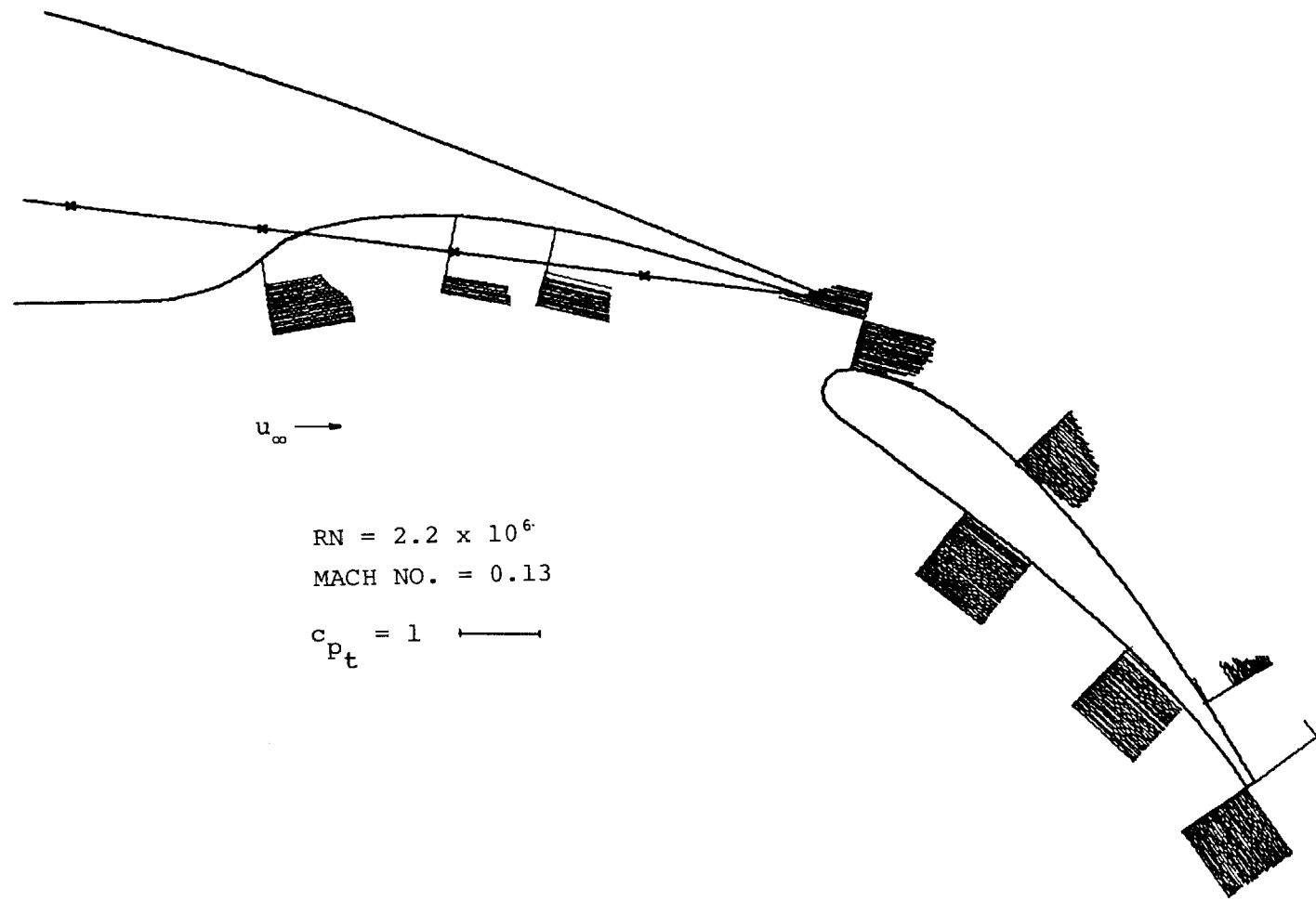
41

(c)  $\alpha = 12.8^\circ$   
 Figure 9 - Concluded.



(a)  $\alpha = 2.7^\circ$

Figure 10 - Total Pressure Profiles.  $\delta_f = 40^\circ$ , Optimum gap.



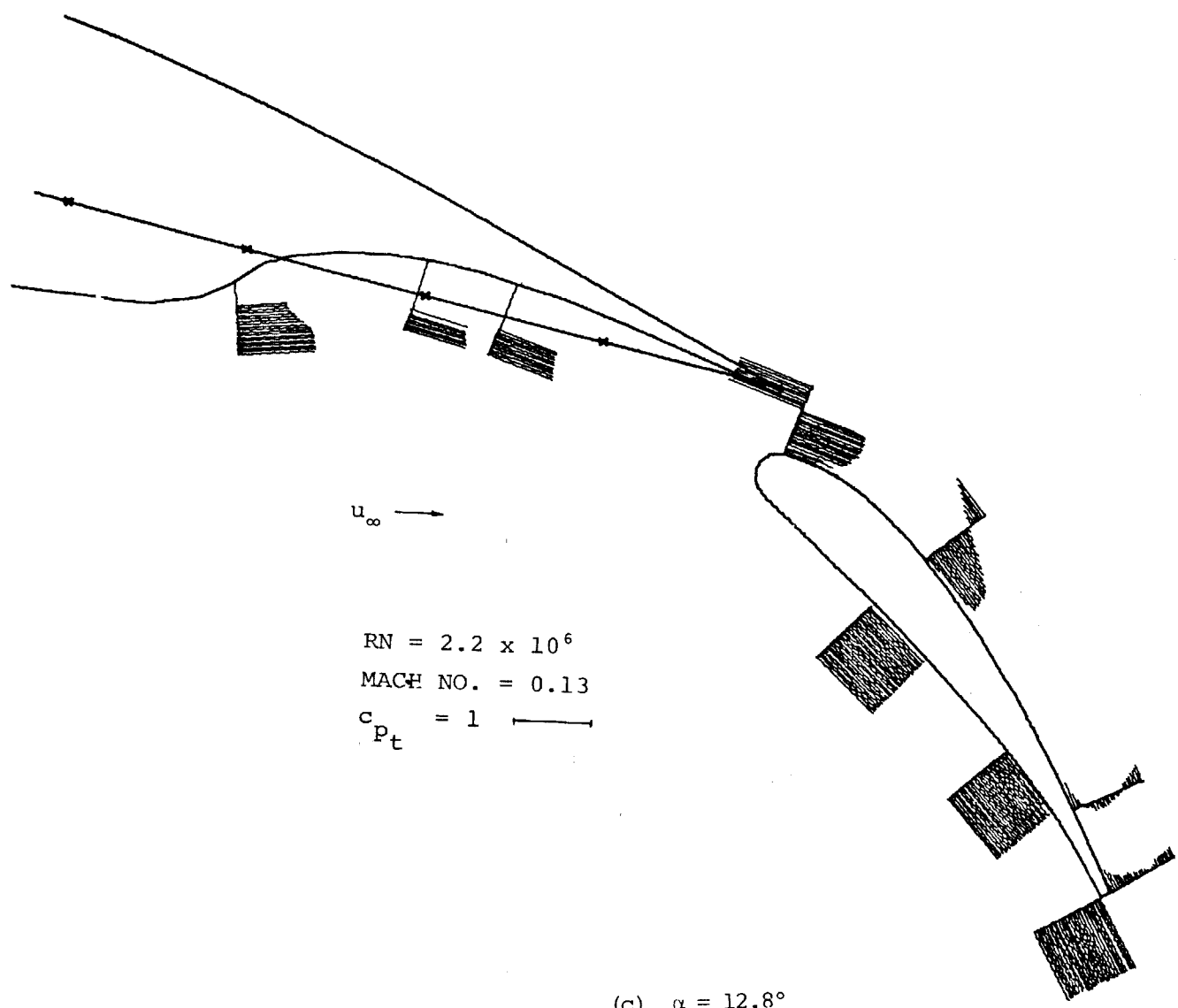
$u_{\infty} \rightarrow$

$RN = 2.2 \times 10^6$   
MACH NO. = 0.13

$c_{p_t} = 1$   $\longleftarrow$

(b)  $\alpha = 7.7^\circ$

Figure 10 - Continued.



$u_\infty \rightarrow$

$RN = 2.2 \times 10^6$

MACH NO. = 0.13

$c_{P_t} = 1$   $\longleftrightarrow$

(c)  $\alpha = 12.8^\circ$

Figure 10 - Concluded.





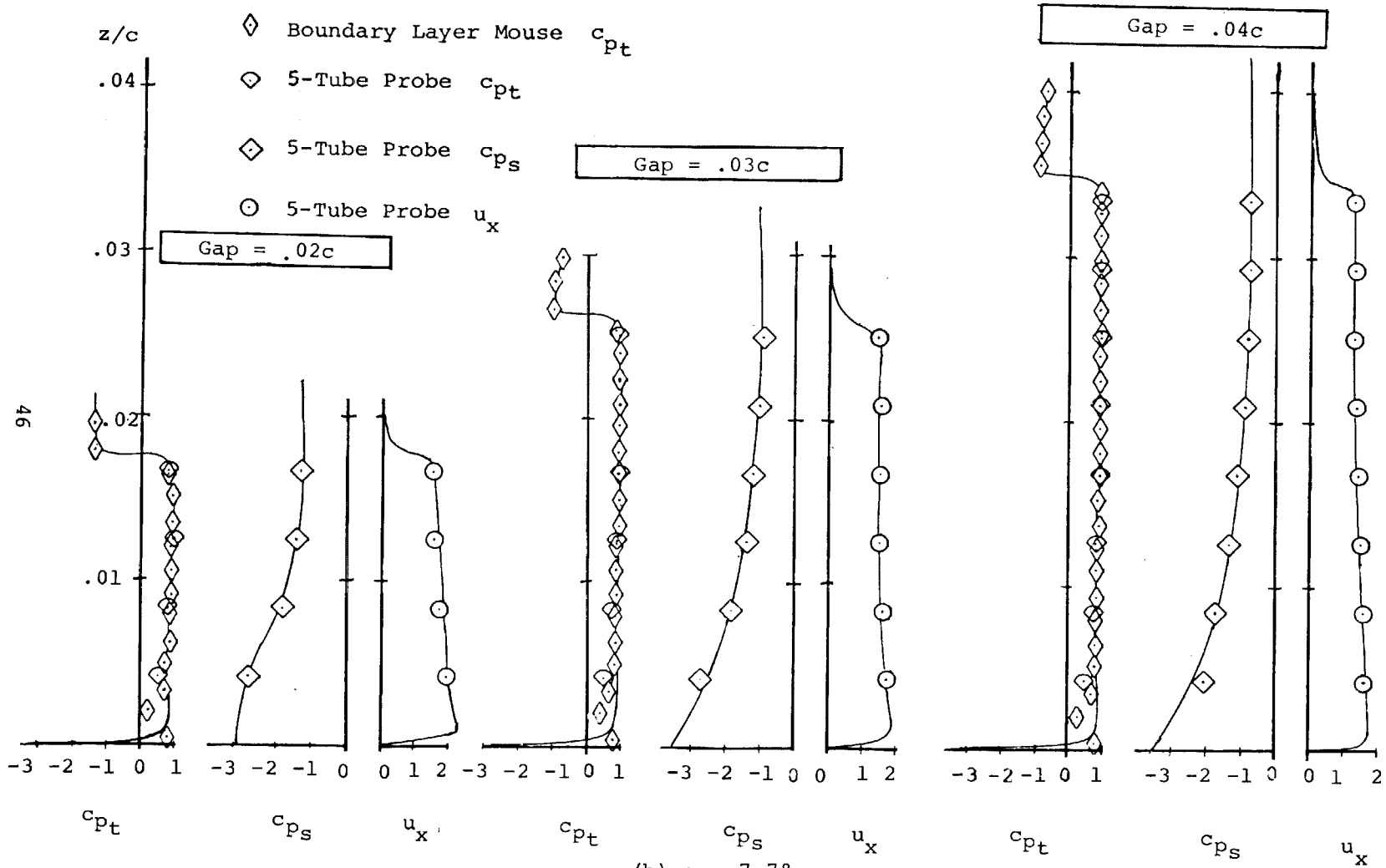
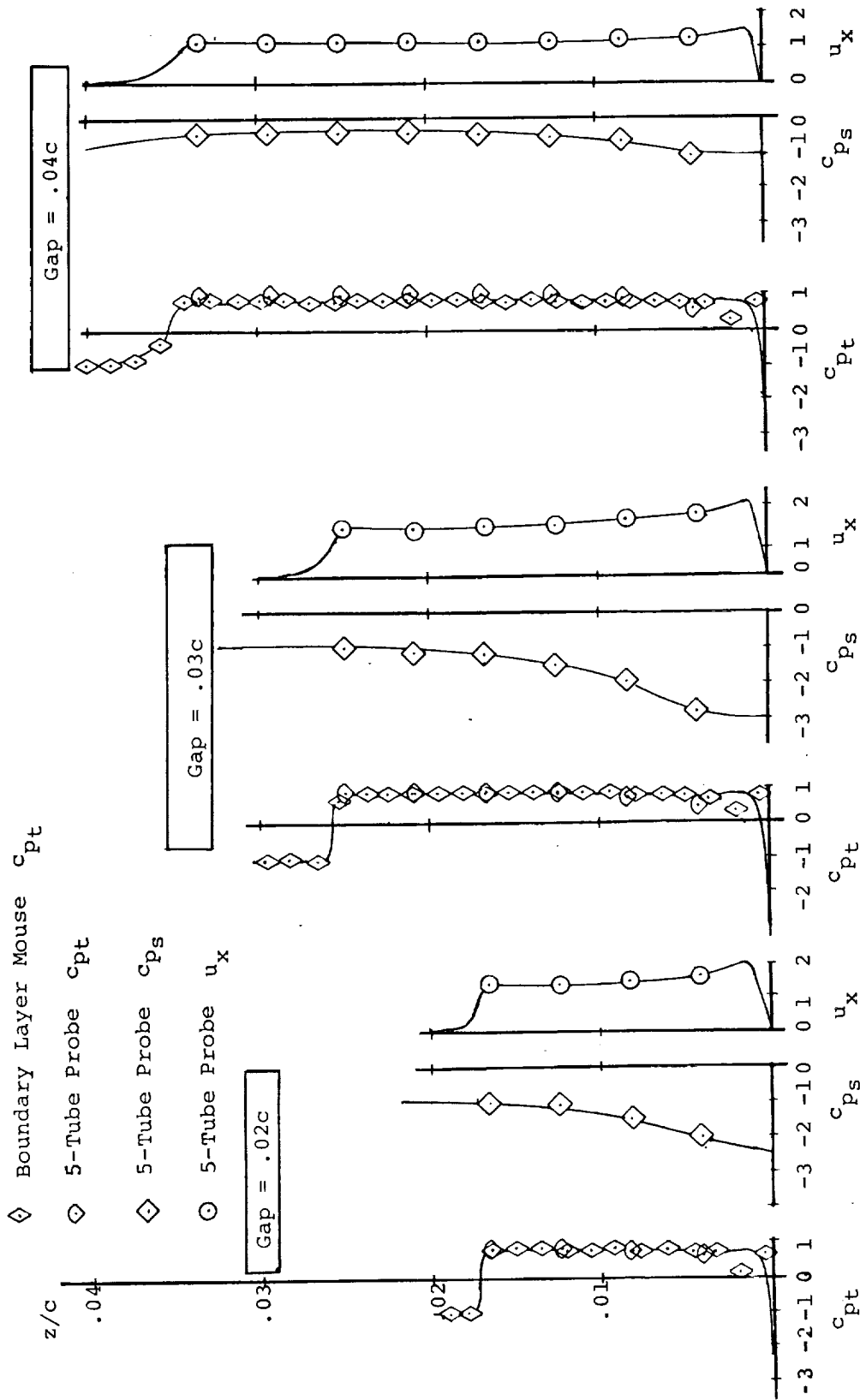
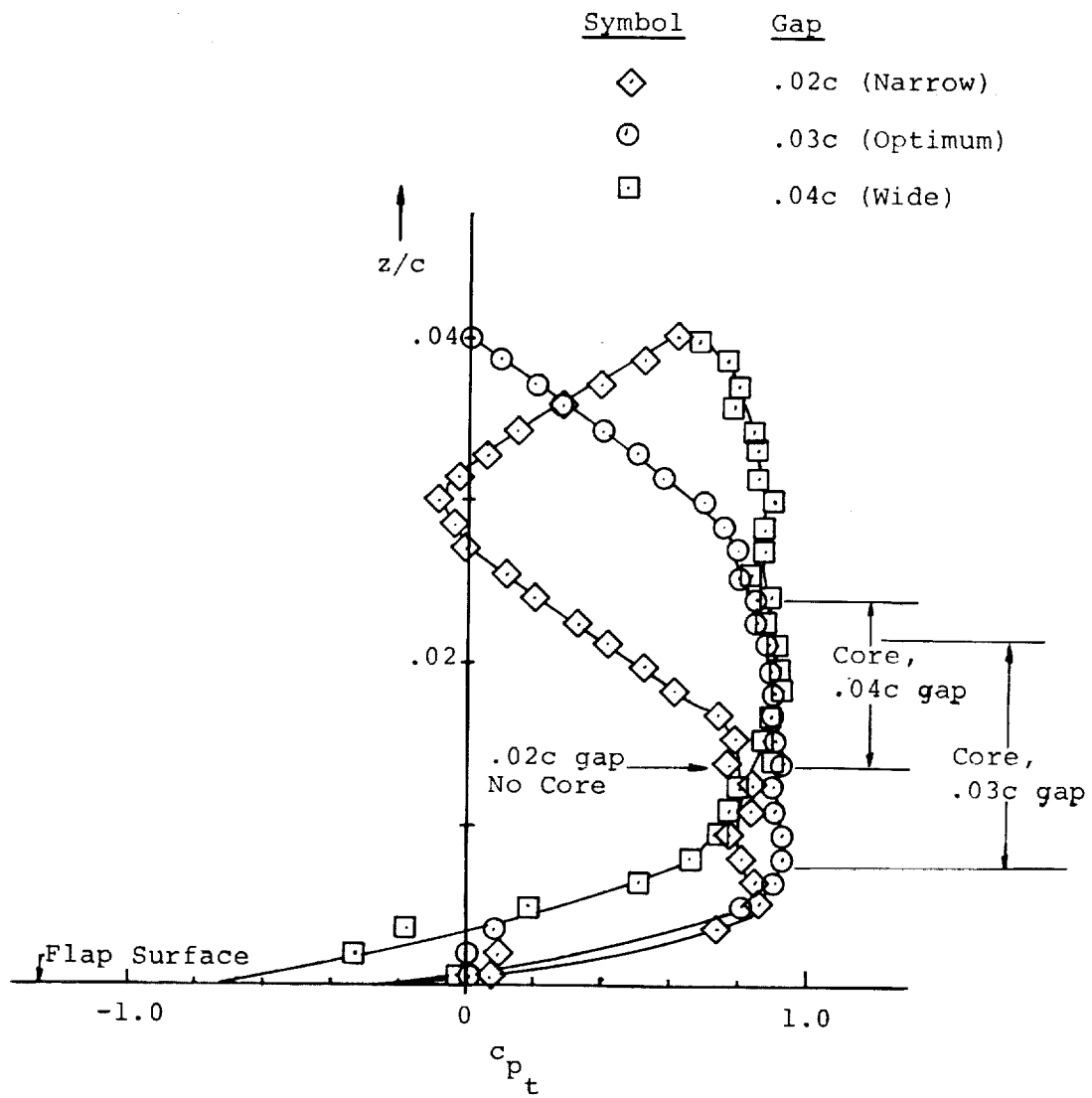


Figure 11 - Continued.

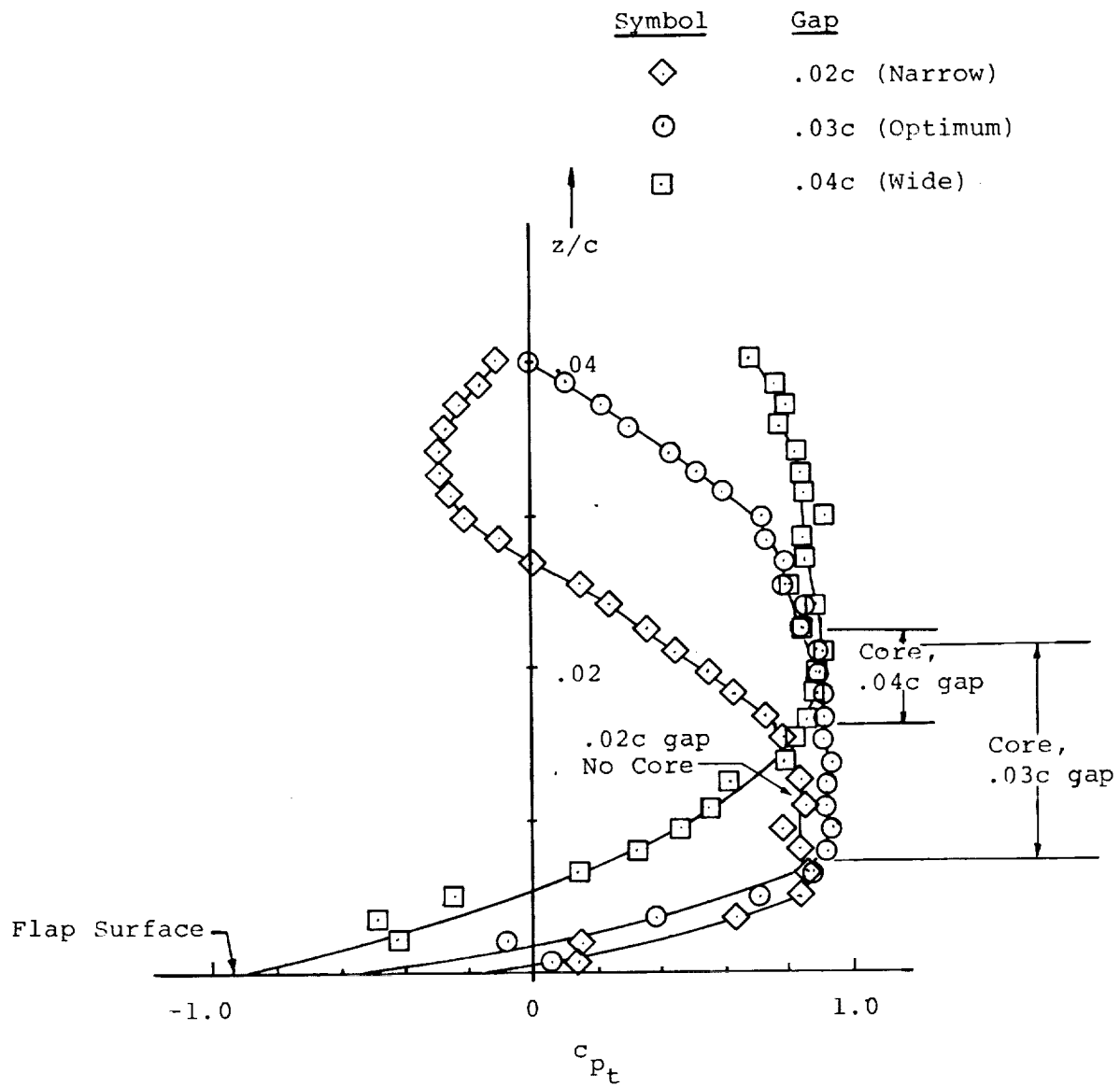


(c)  $\alpha = 12.7^\circ$

Figure 11 - Concluded.

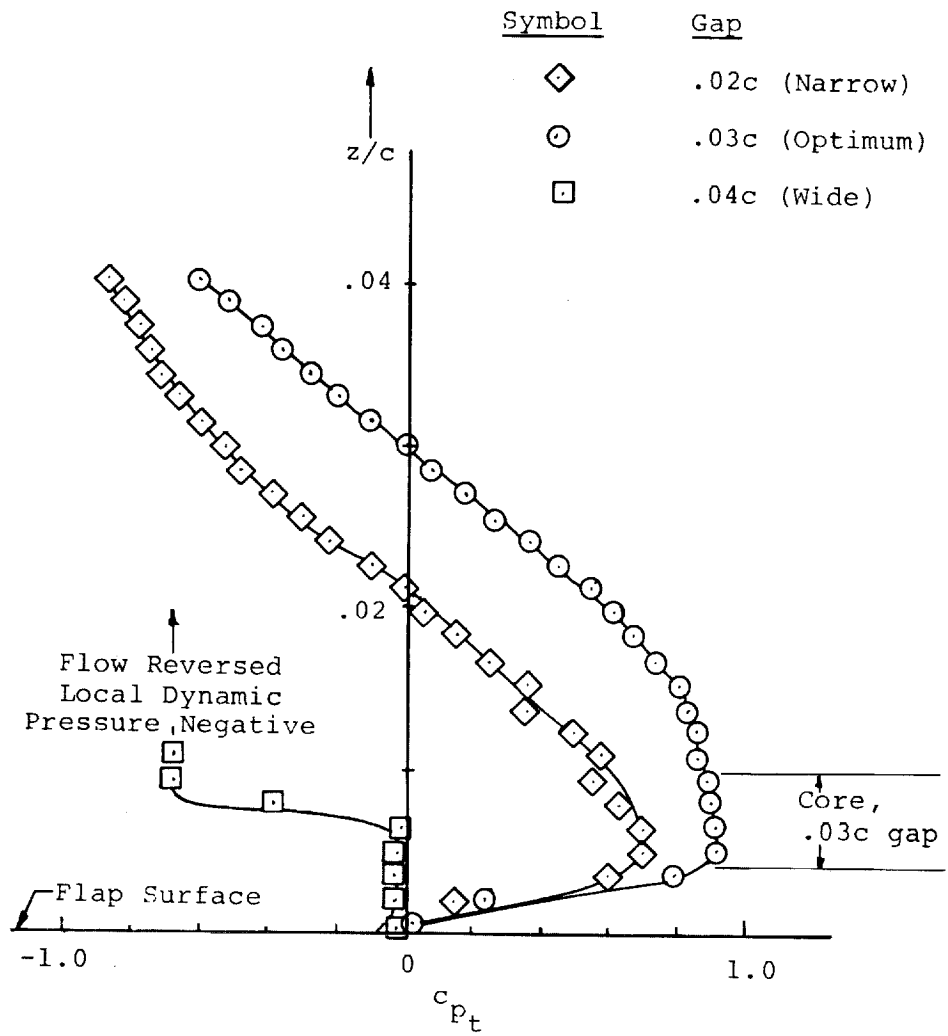


(a)  $\alpha = 2.7^\circ$   
 Figure 12 - Effect of Gap on Total Pressure Downstream of the Slot Exit.  $\delta_f = 40^\circ$ ,  $x_f/c = 0.10$ .



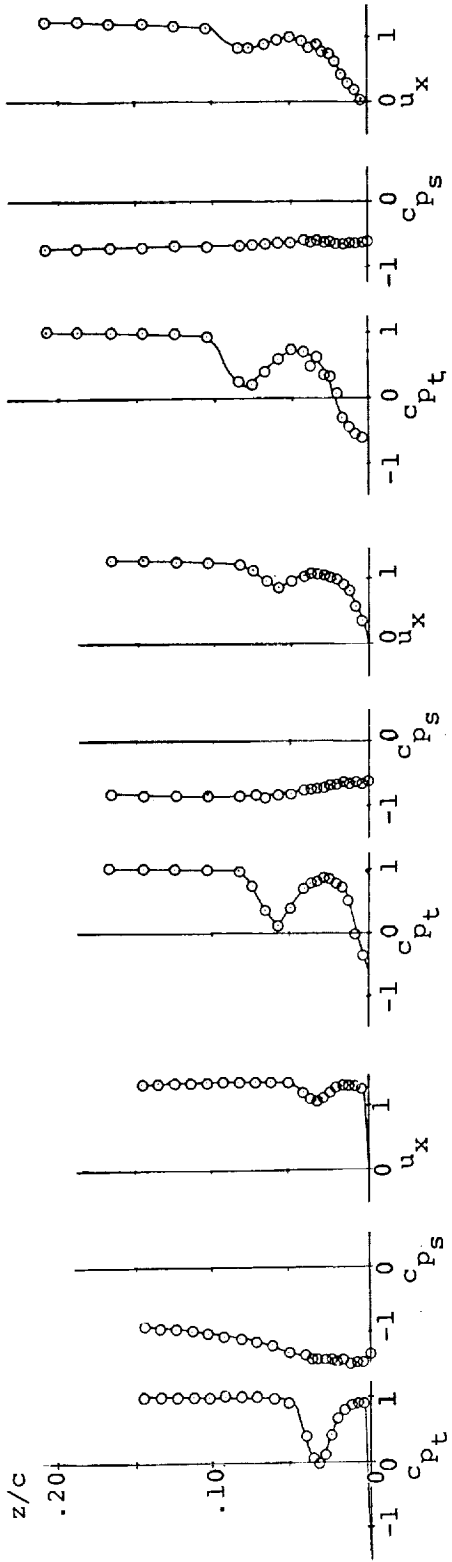
(b)  $\alpha = 7.7^\circ$

Figure 12 - Continued.



(c)  $\alpha = 12.8^\circ$

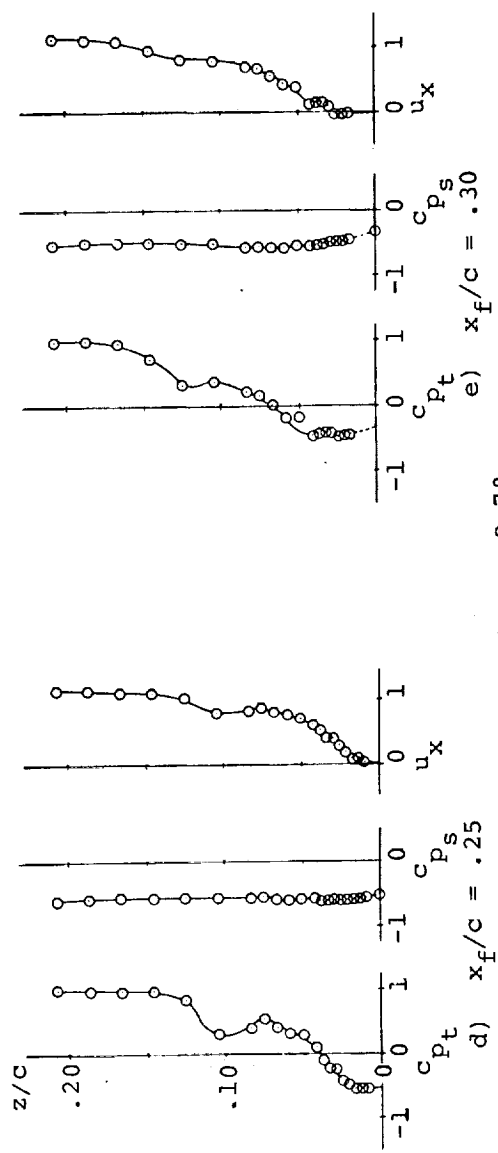
Figure 12 - Concluded.



a)  $x_f/c = .075$

b)  $x_f/c = .15$

c)  $x_f/c = .20$

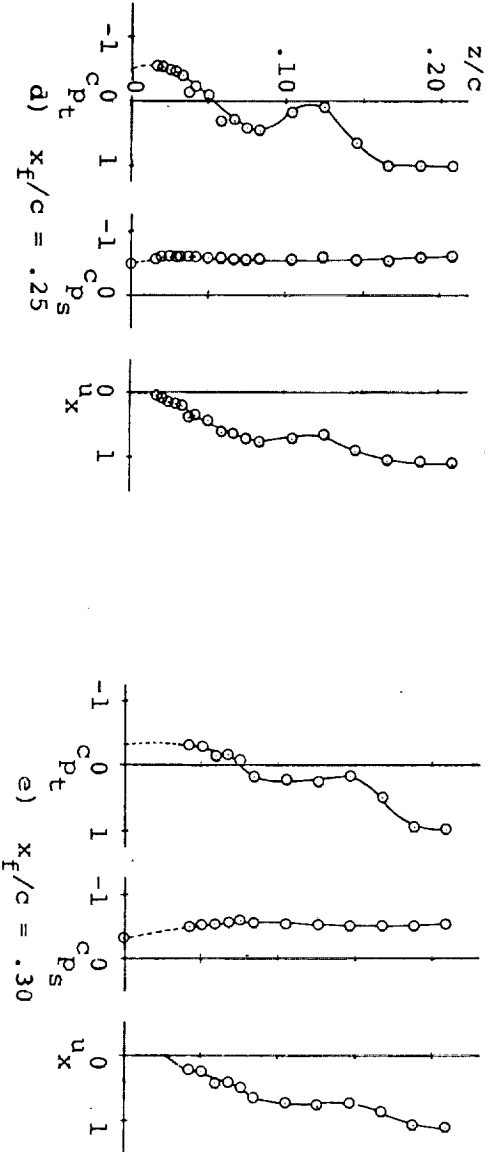
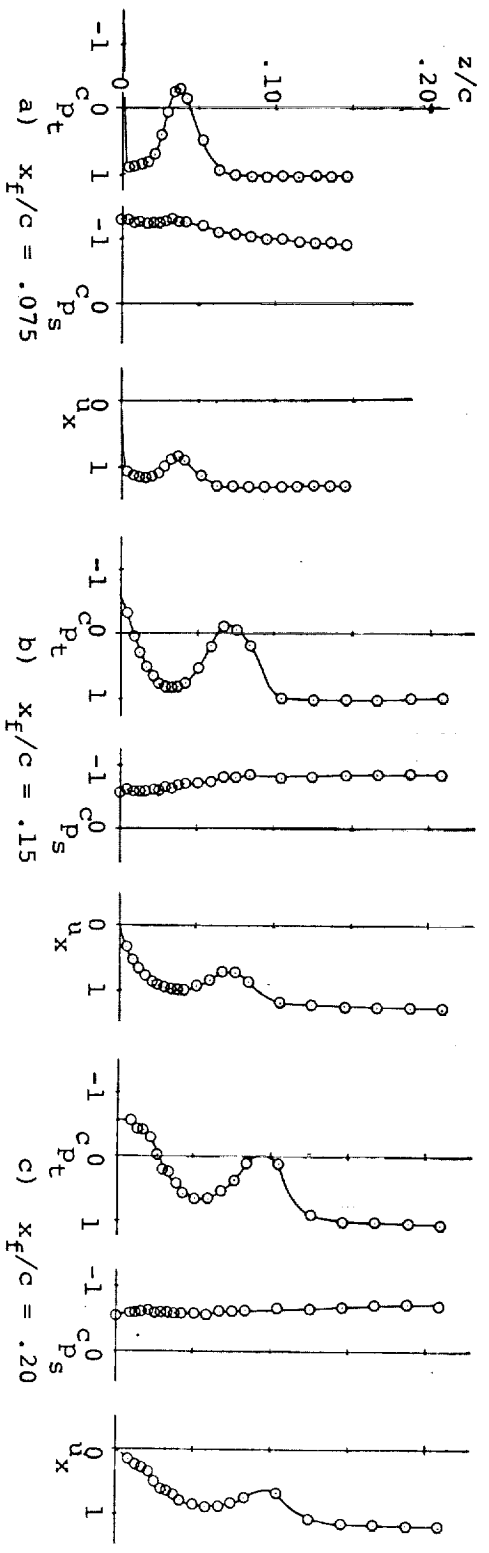


d)  $x_f/c = .25$

e)  $x_f/c = .30$

(a)  $\alpha = 2.7^\circ$

Figure 13 - Velocity and Pressure Distributions on the Flap.  
 $\delta_f = 40^\circ$ , Optimum gap.



(b)  $\alpha = 7.7^\circ$

Figure 13 - Continued.



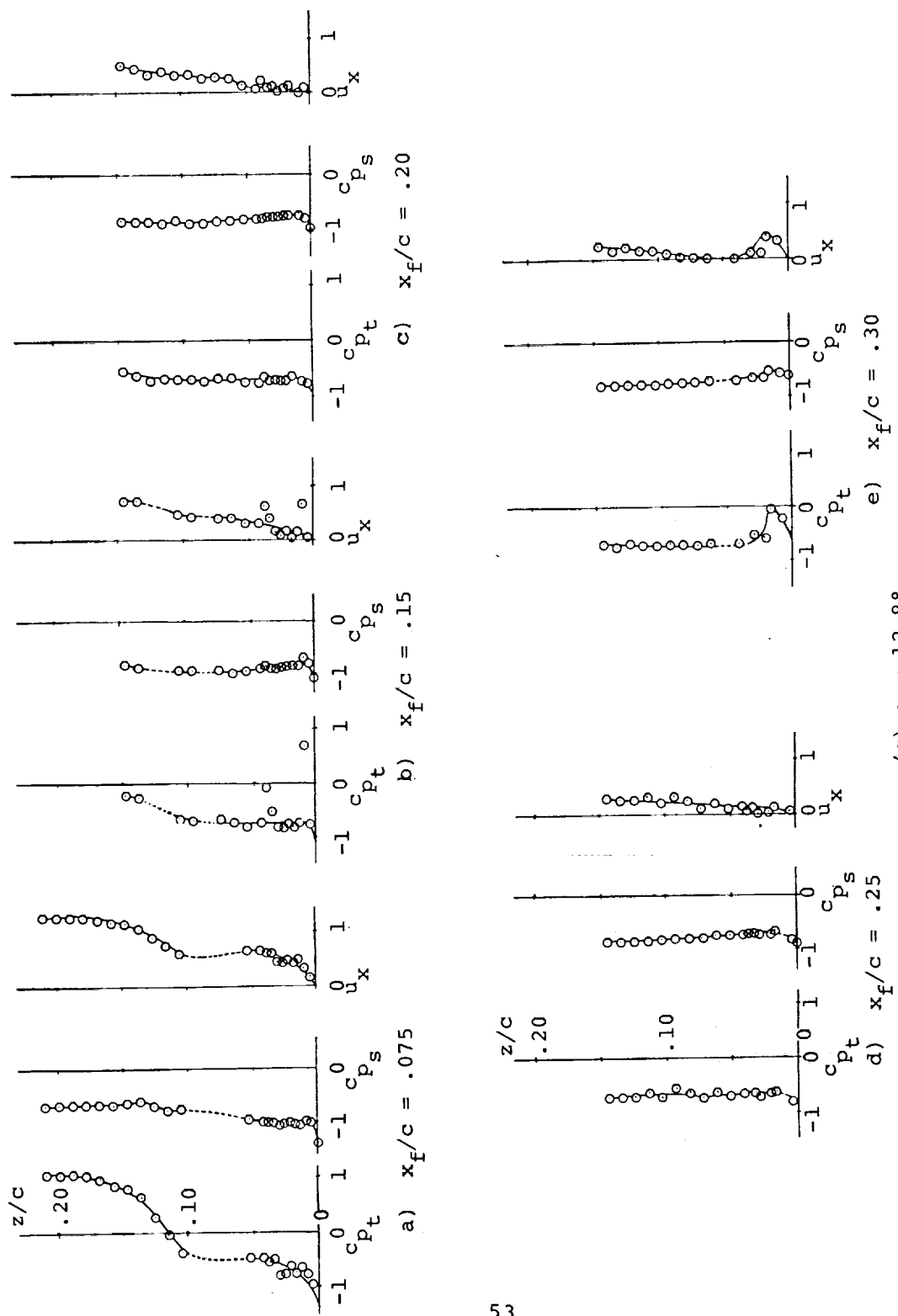
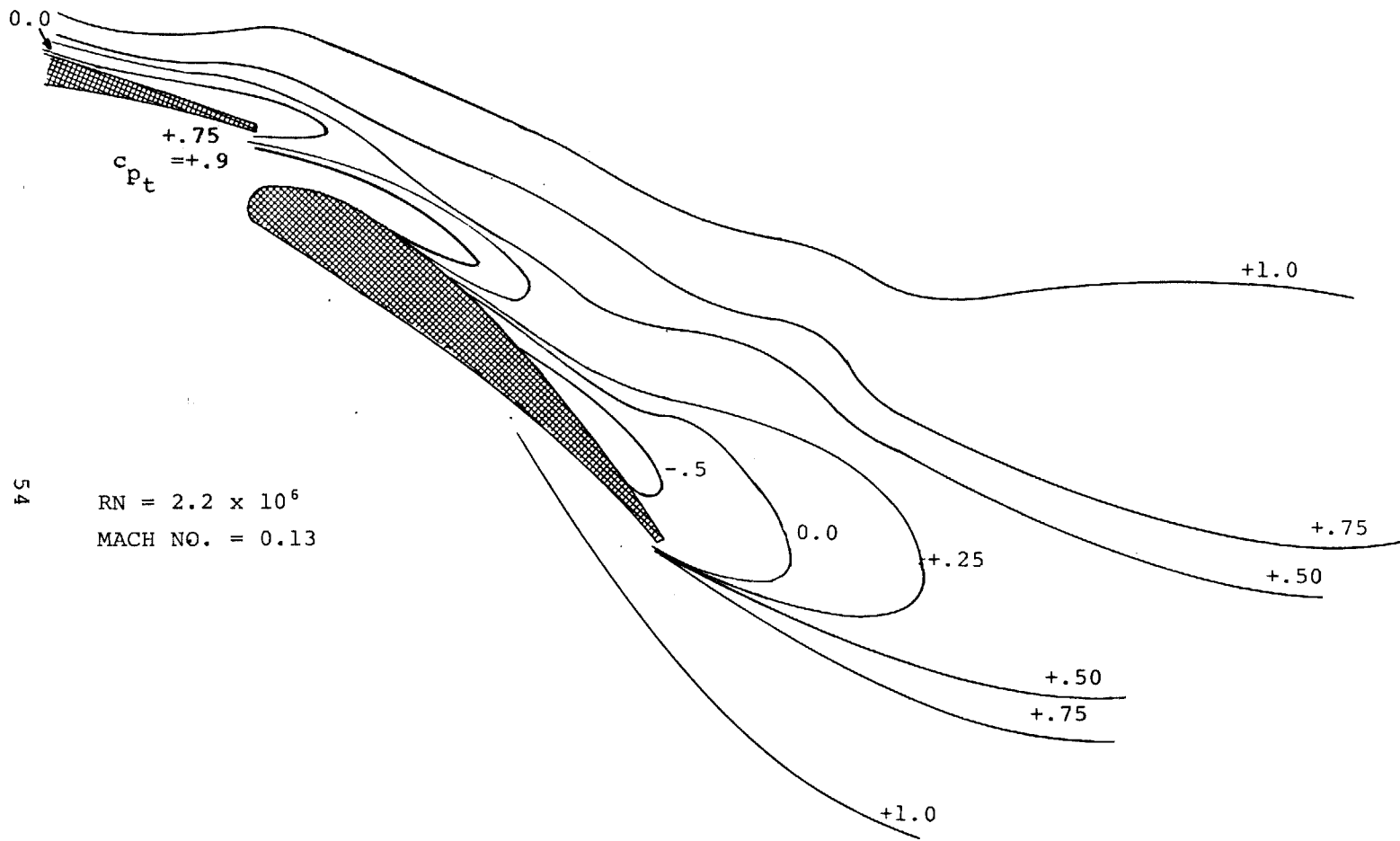
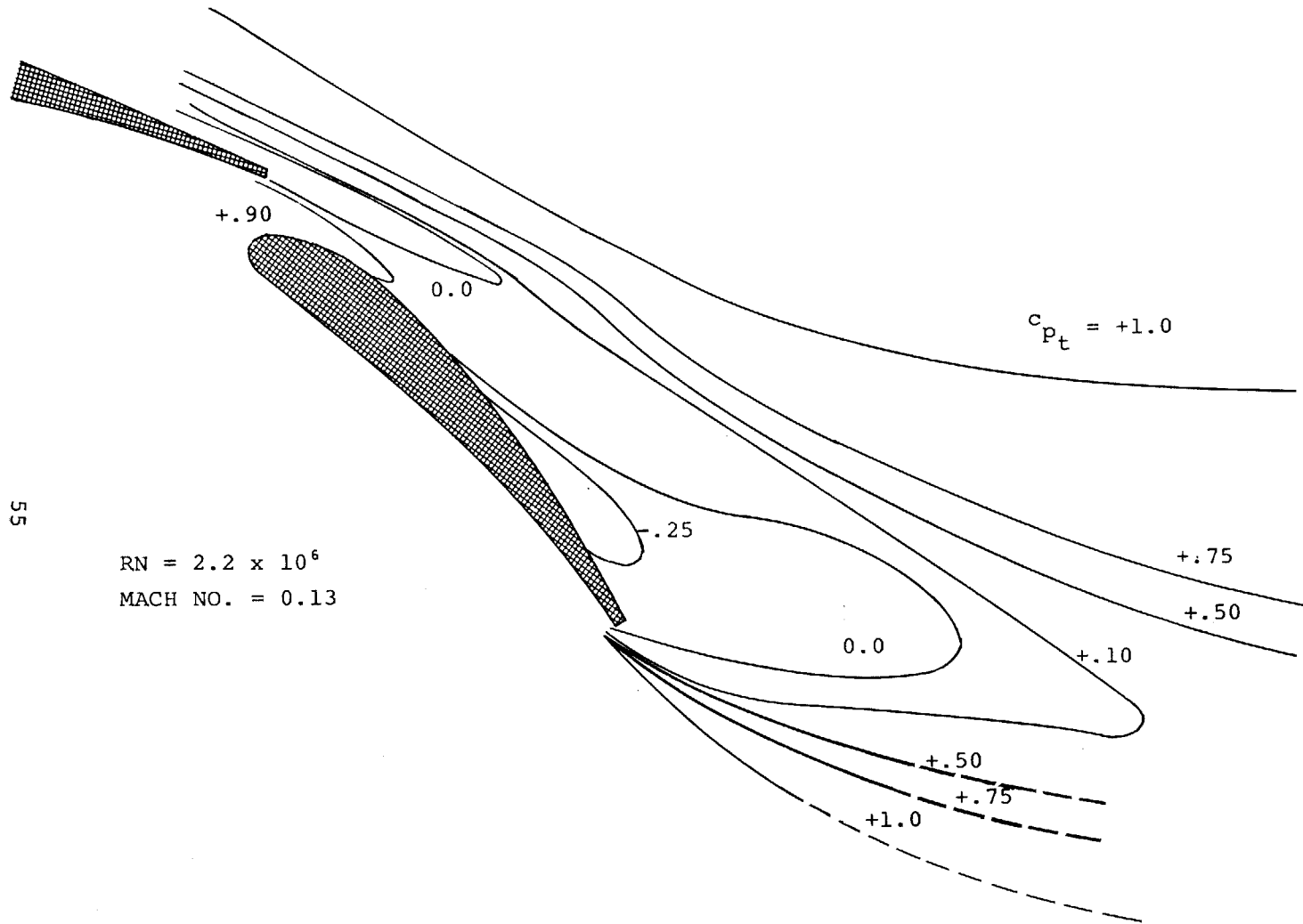


Figure 13 - Concluded.



(a)  $\alpha = 2.7^\circ$

Figure 14 - Total Pressure Contours.  $\delta_f = 40^\circ$ , Optimum gap.

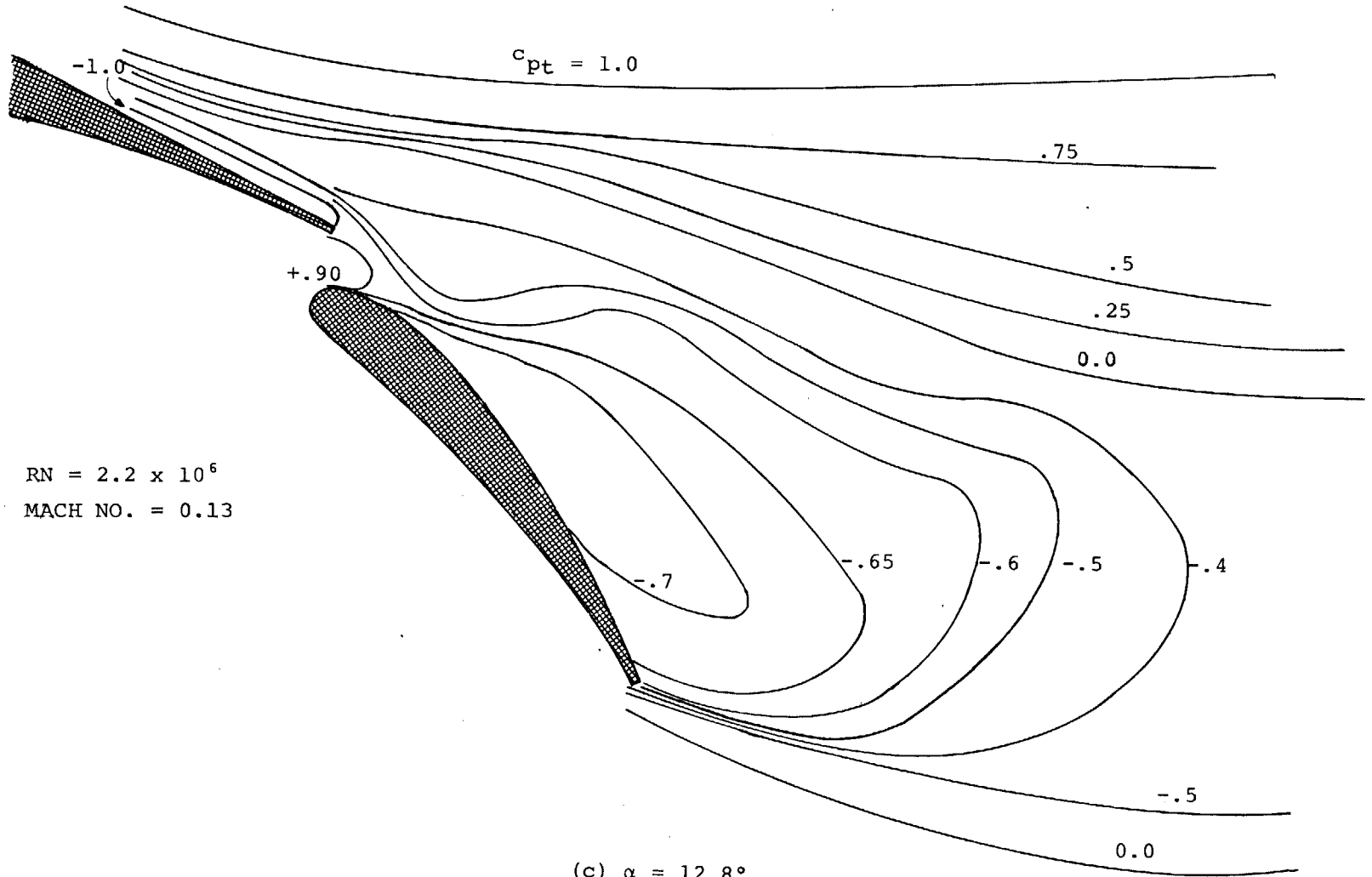


55

RN =  $2.2 \times 10^6$   
MACH NO. = 0.13

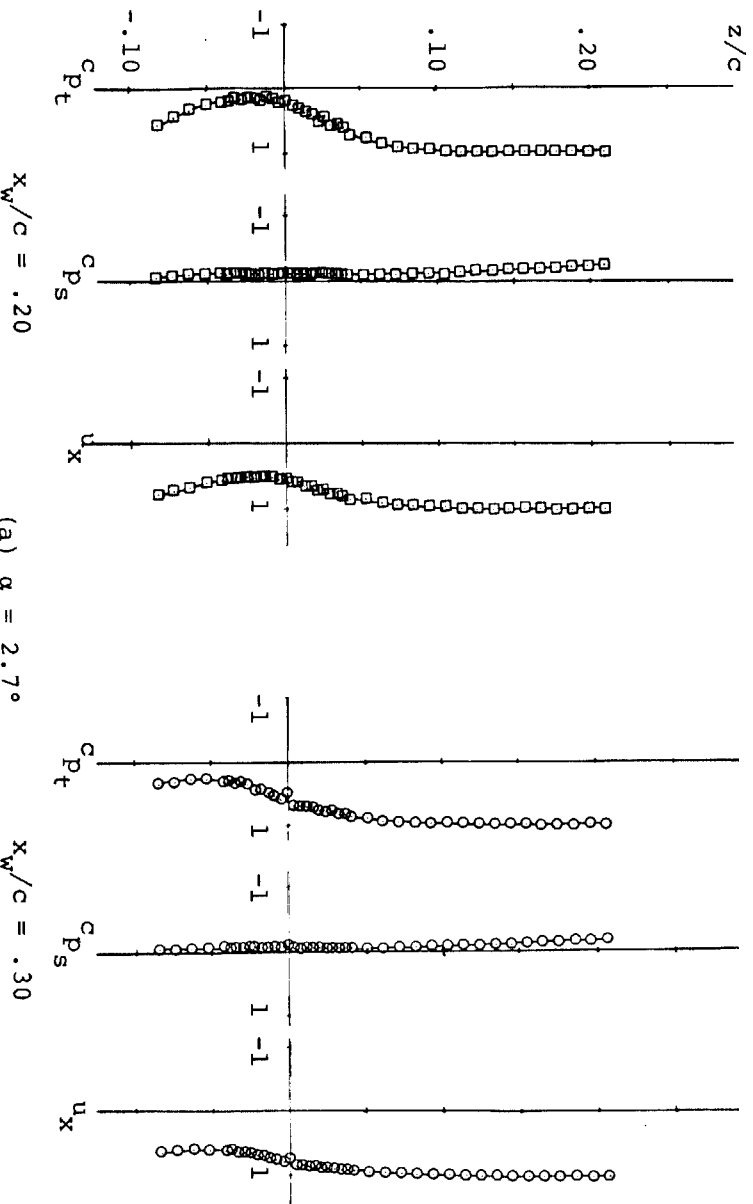
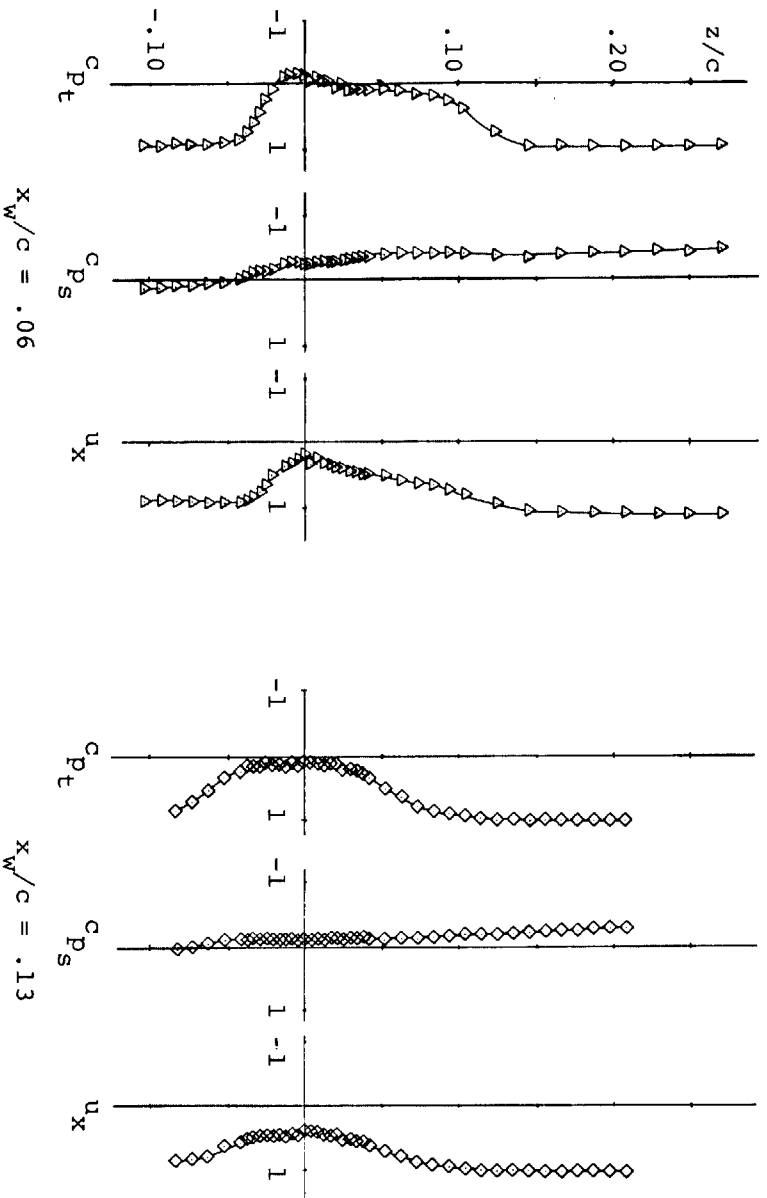
(b)  $\alpha = 7.7^\circ$

Figure 14 - Continued.



RN =  $2.2 \times 10^6$   
MACH NO. = 0.13

(c)  $\alpha = 12.8^\circ$   
Figure 14 - Concluded.



(a)  $\alpha = 2.7^\circ$   
 Figure 15 - Velocity and Pressure Distributions in the Wake.  $\delta_f = 40^\circ$ , Optimum gap.

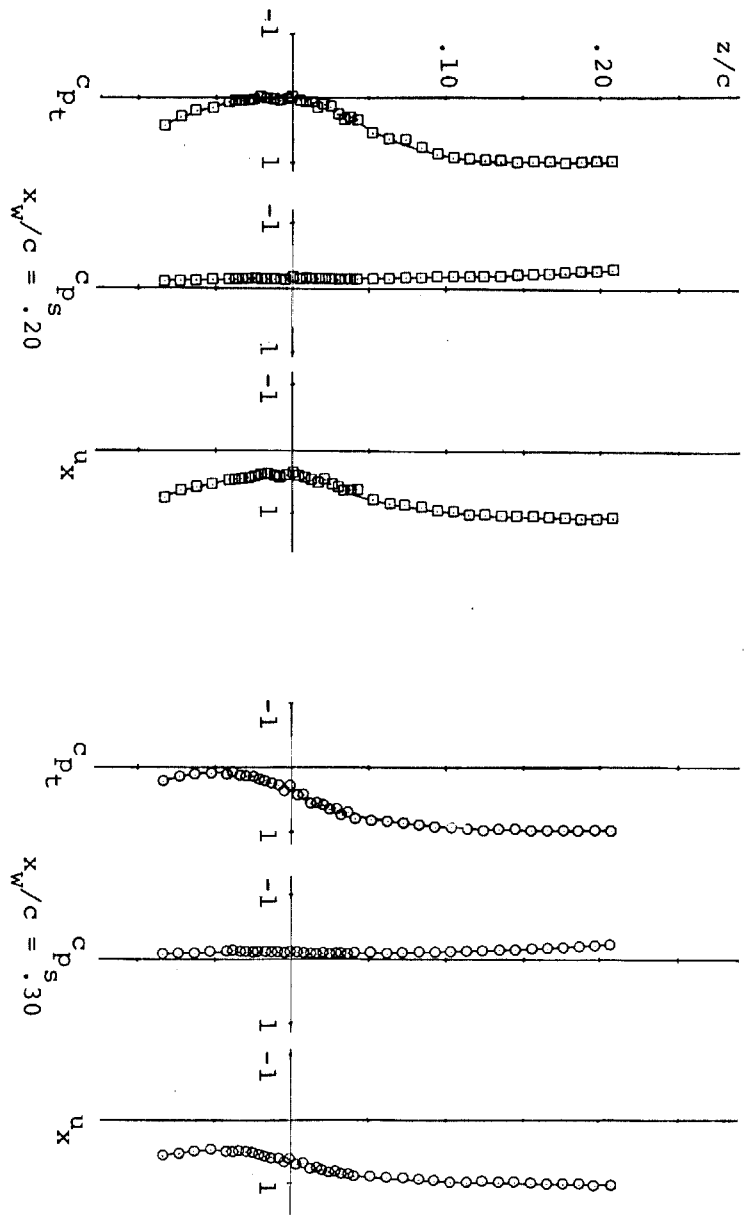
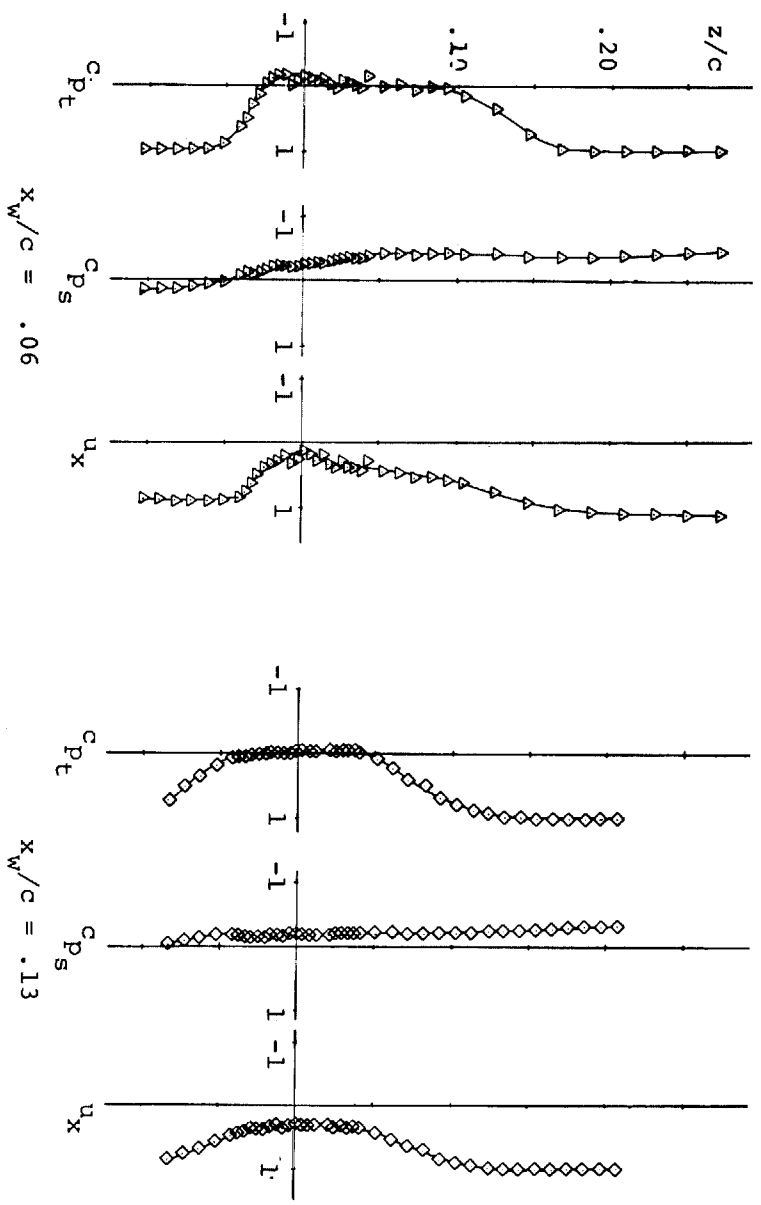


Figure 15 - Continued.

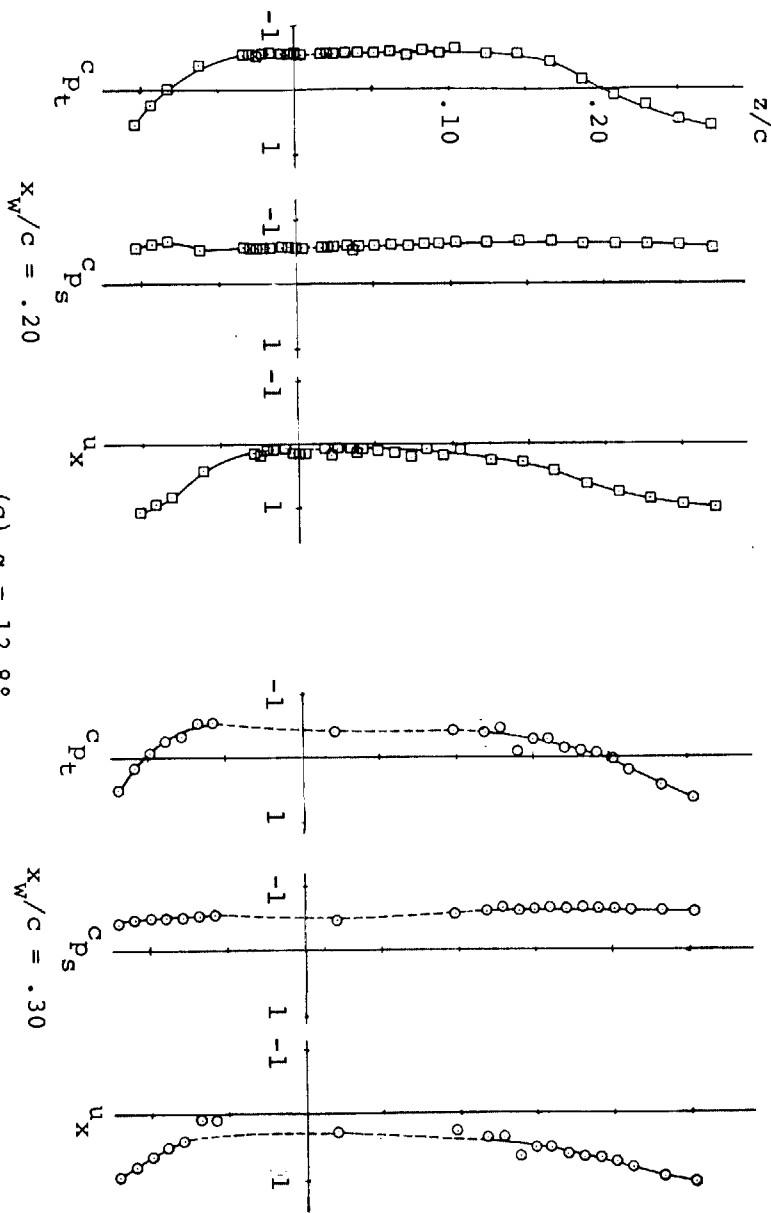
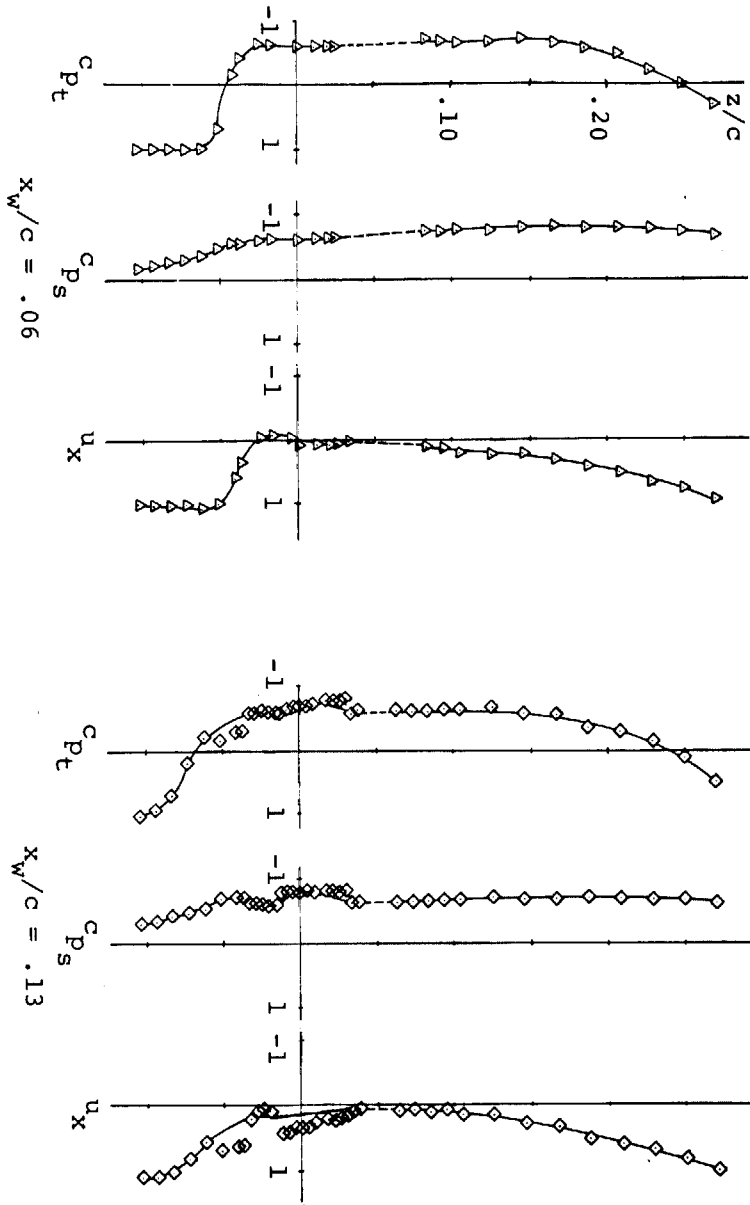
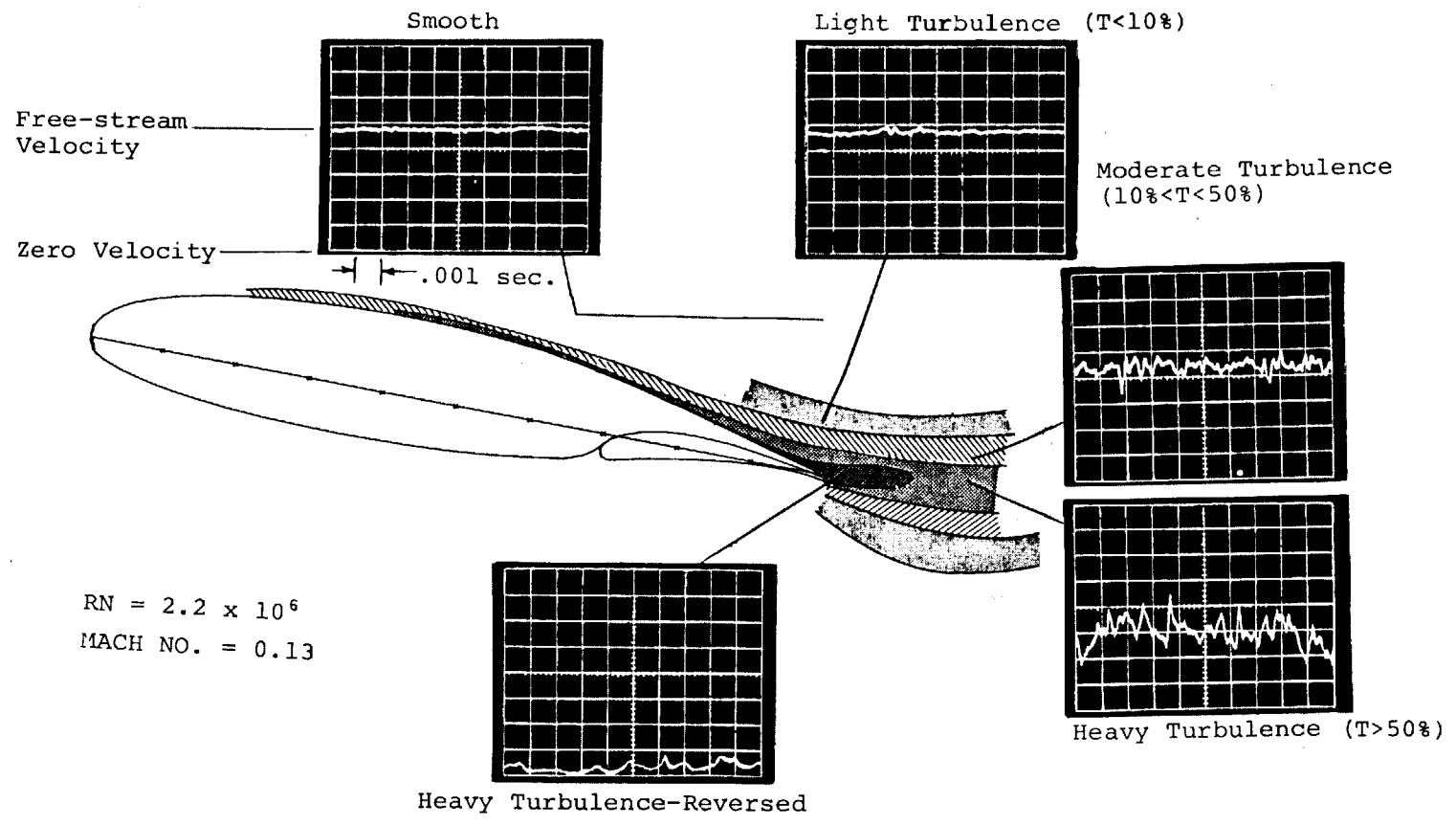


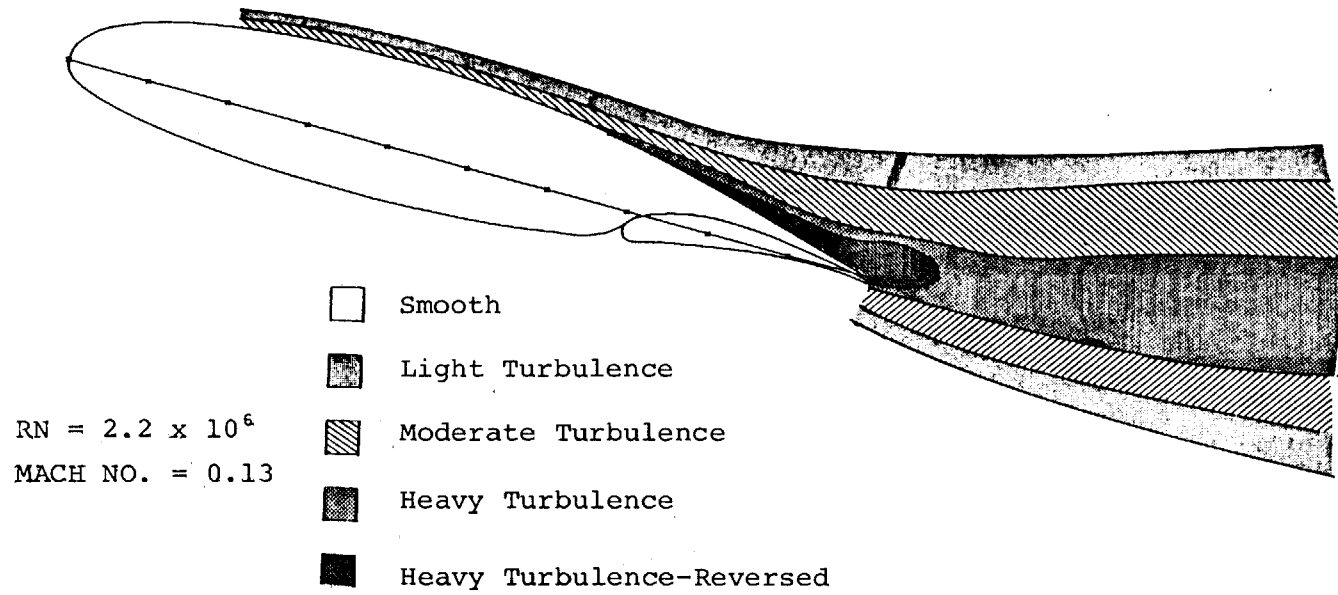
Figure 15 - Concluded.



(a)  $\alpha = 10.3^\circ$

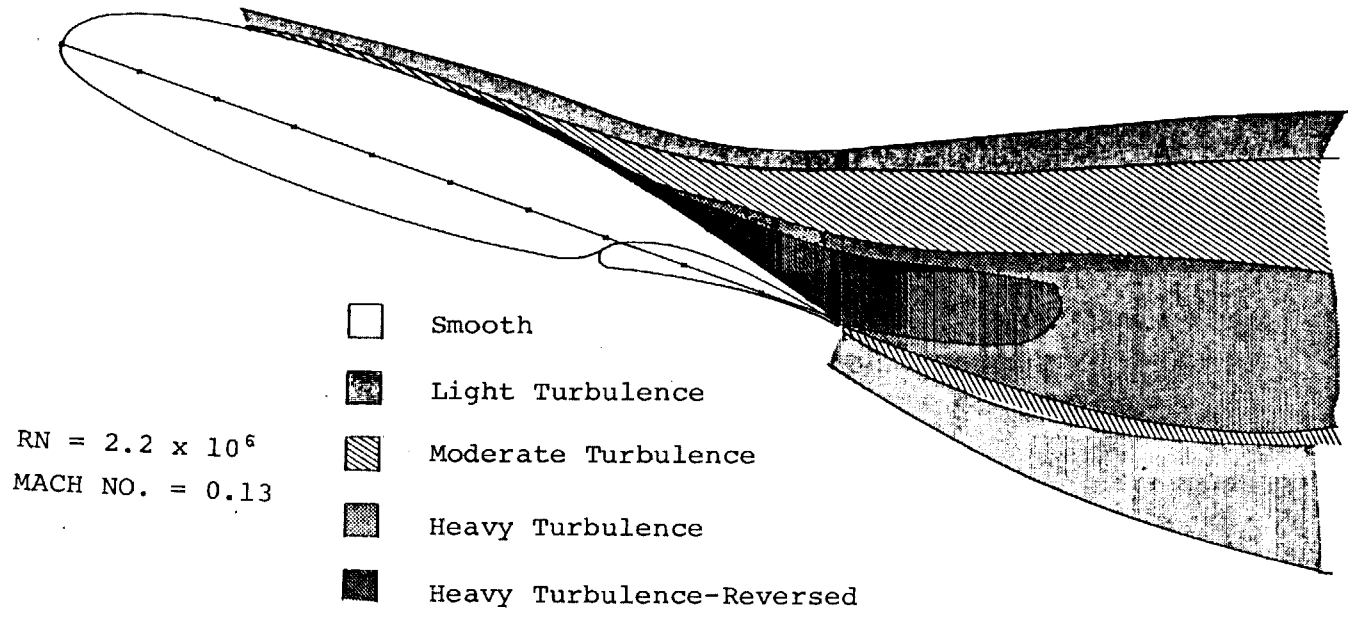
Figure 16 - Hot Film Survey. Flap Retracted.





(b)  $\alpha = 14.4^\circ$

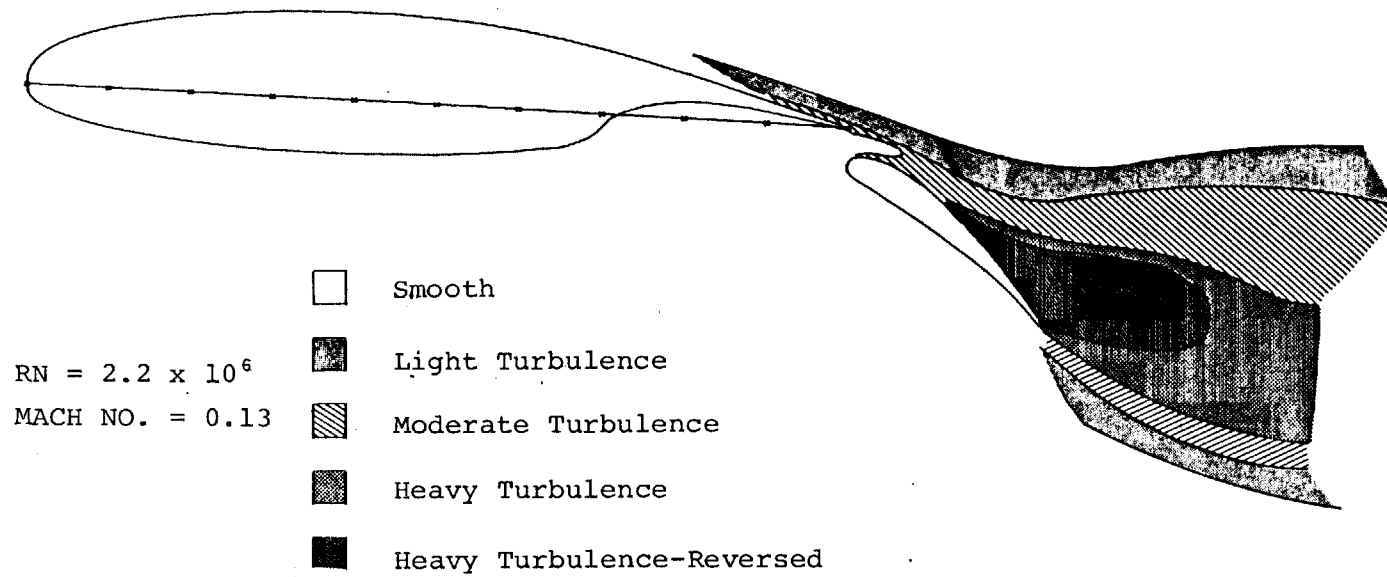
Figure 16 - Continued.



RN =  $2.2 \times 10^6$   
MACH NO. = 0.13

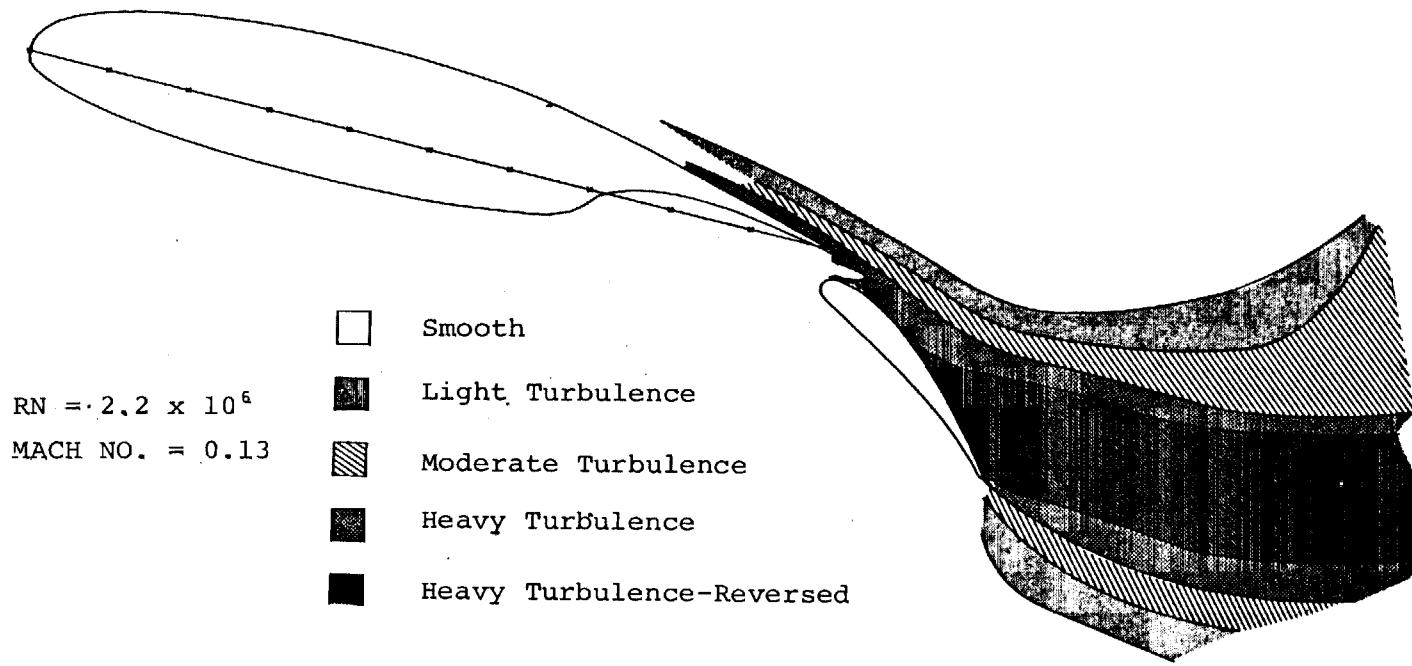
(c)  $\alpha = 18.4^\circ$

Figure 16 - Concluded.



(a)  $\alpha = 2.7^\circ$

Figure 17 - Hot Film Survey.  $\delta_f = 40^\circ$ , Optimum gap.



(b)  $\alpha = 12.8^\circ$

Figure 17 - Concluded.

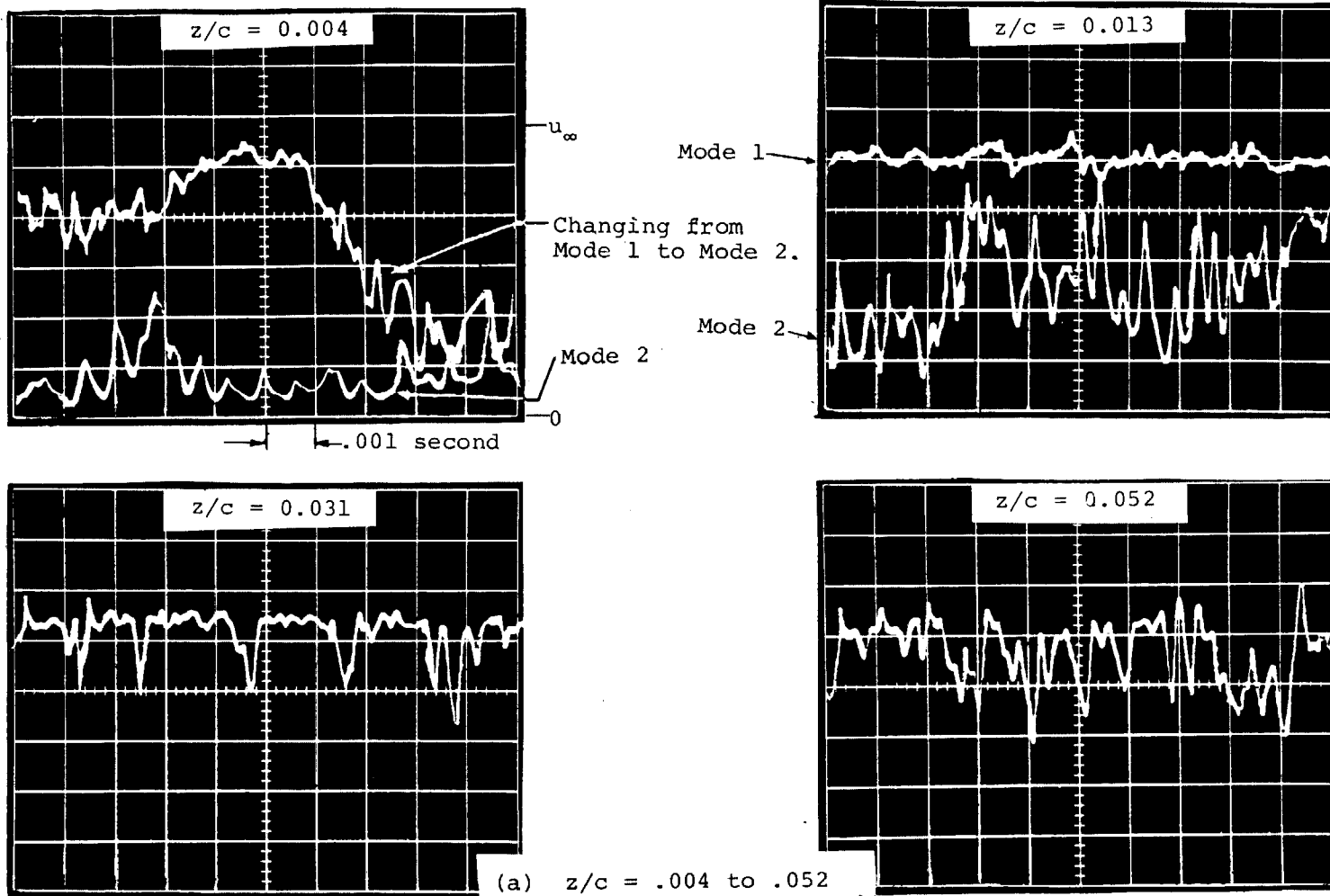
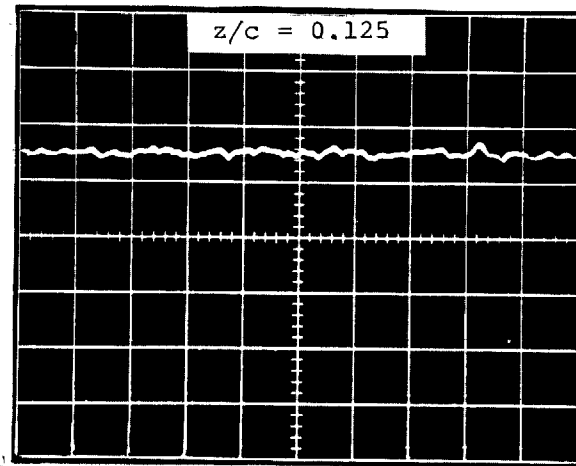
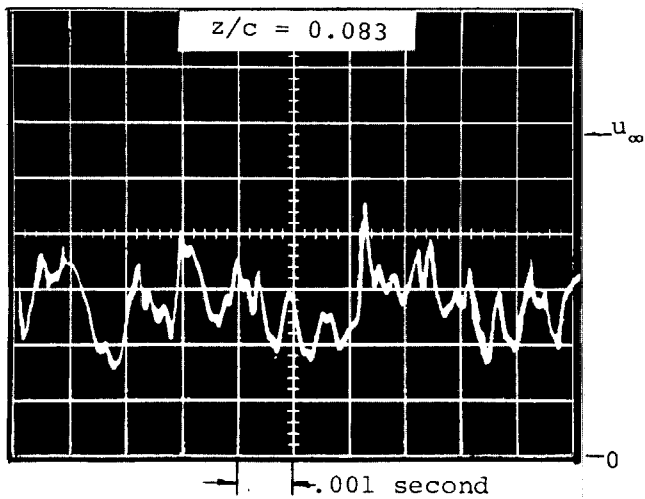


Figure 18 - Hot Film Survey on the Flap.  $\delta_f = 40^\circ$ , Optimum gap,  $\alpha = 12.8^\circ$ ,  $x_f/c = .15$ .



(b)  $z/c = .083$  and  $.125$ .

Figure 18 - Concluded.

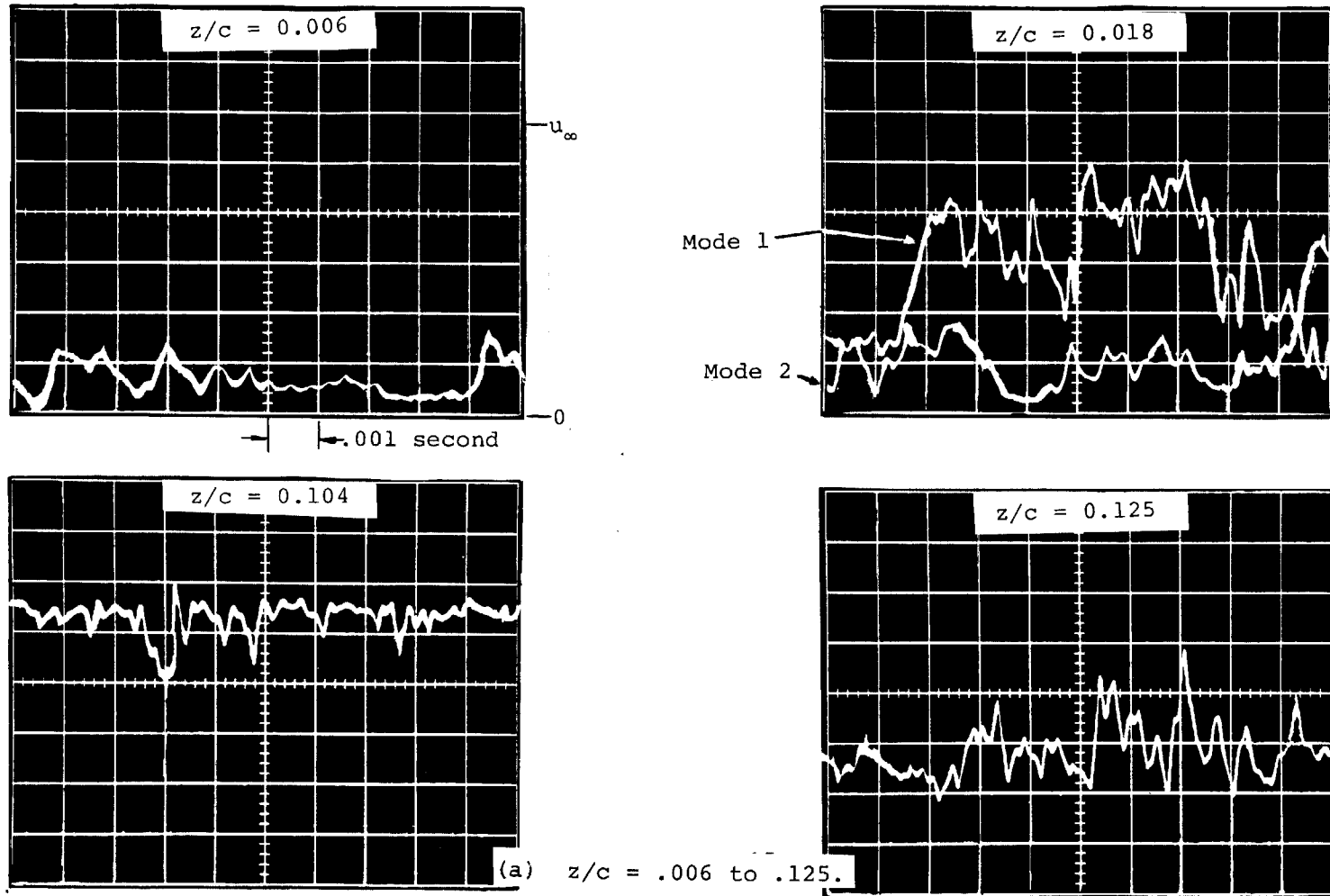
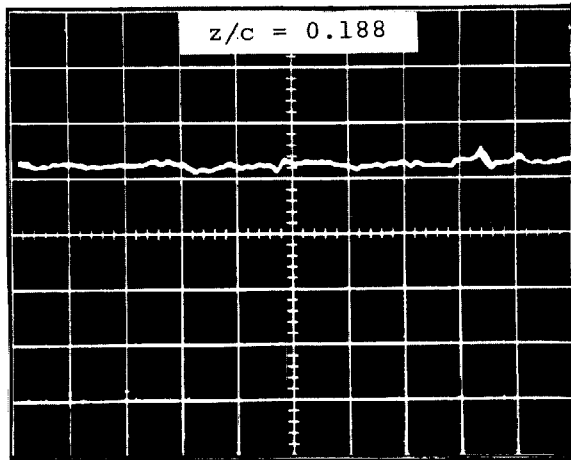
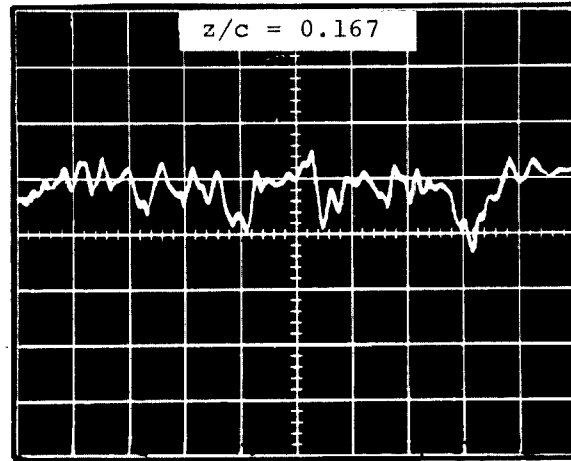
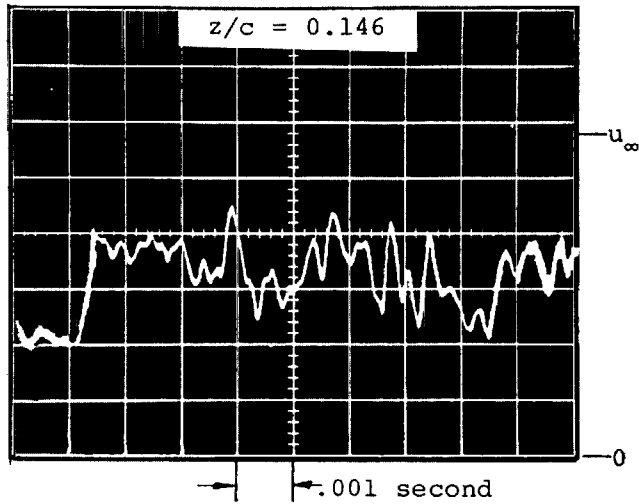


Figure 19 - Hot-Film Survey on the Flap.  $\delta_f = 40^\circ$ , Optimum gap,  $\alpha = 12.8^\circ$ ,  $x_f/c = .25$ .



(b)  $z/c = .146$  to  $.188$   
Figure 19 - Concluded.



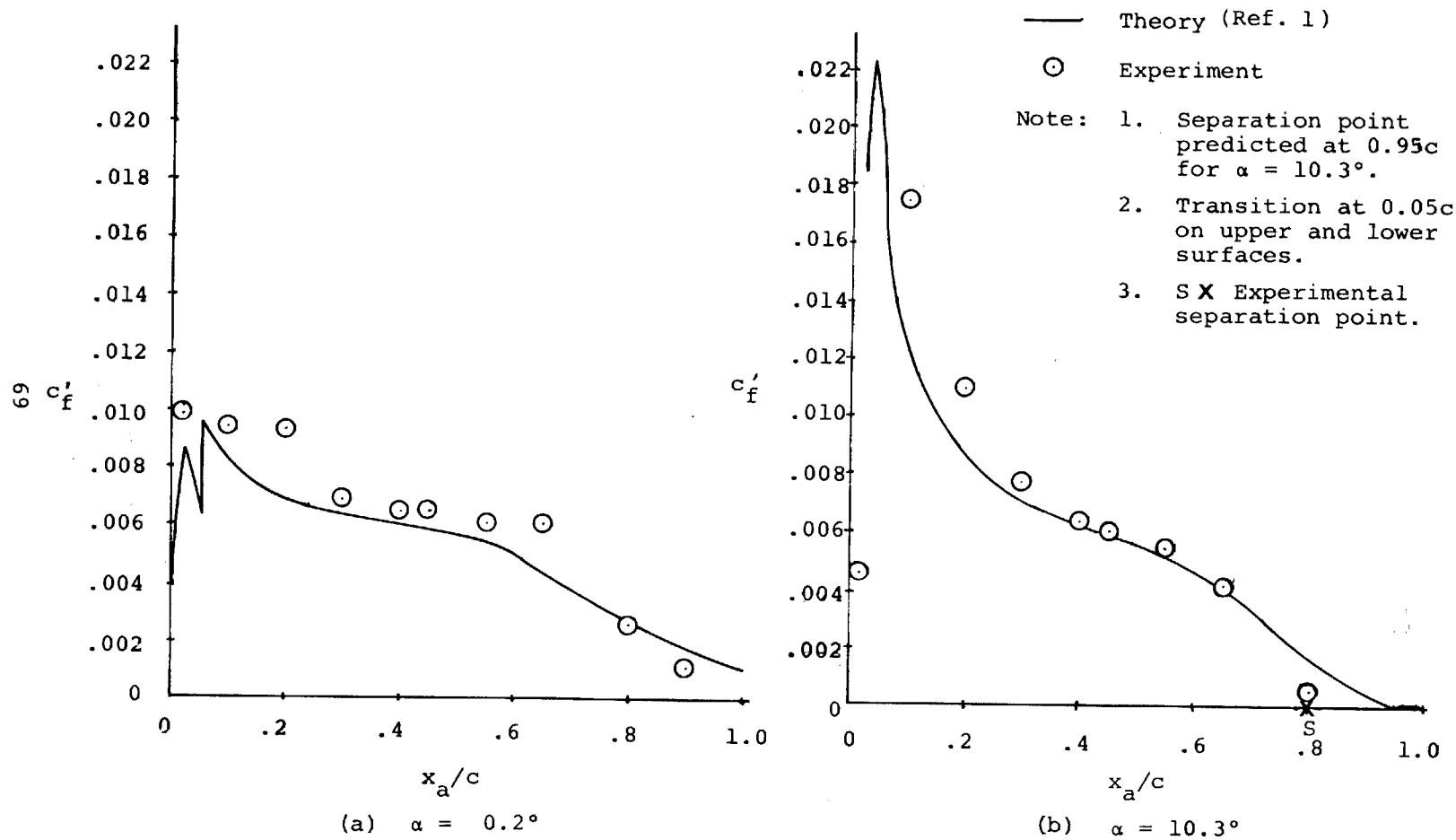
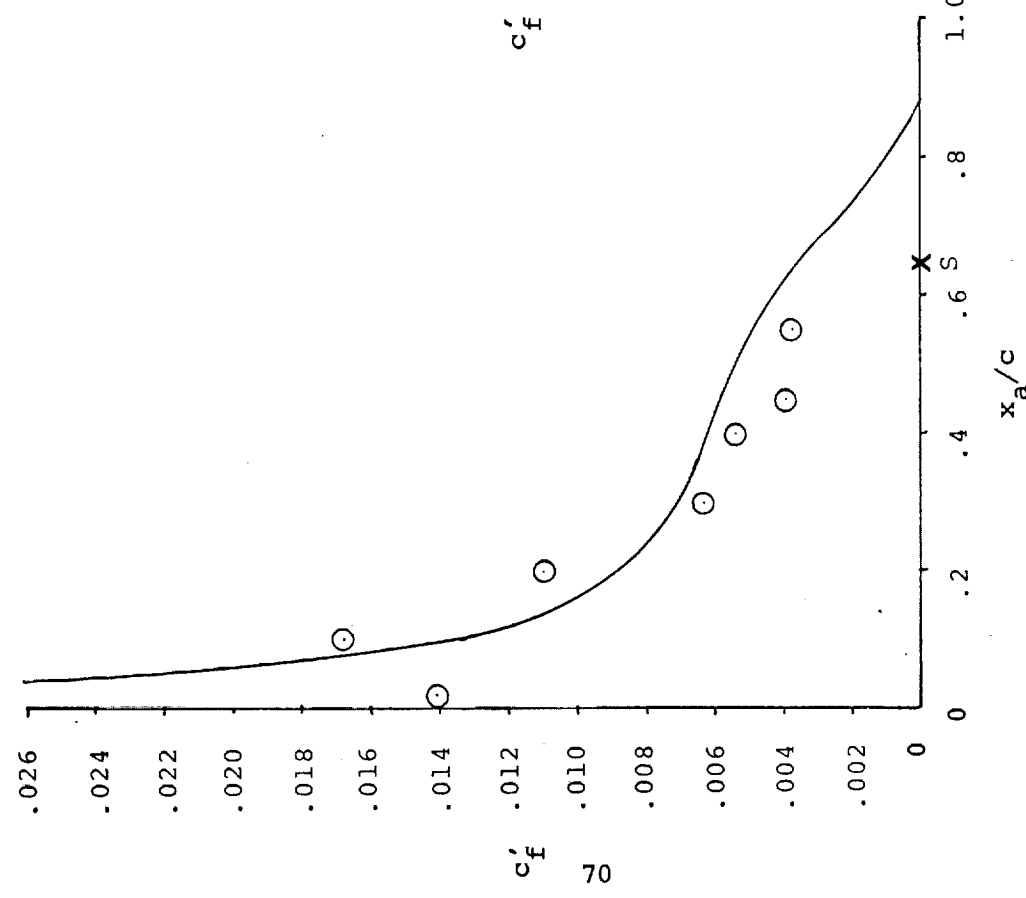
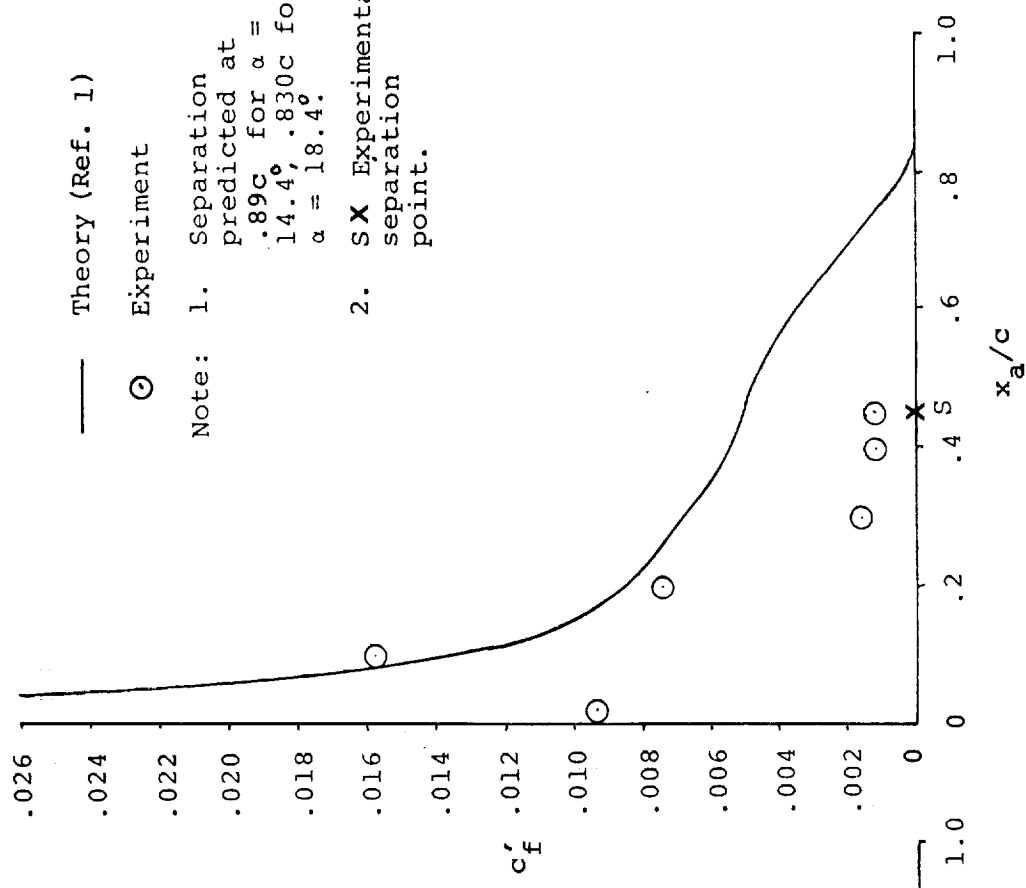


Figure 20 - Comparison of Experimental and Theoretical Skin Friction Distributions. Flap Retracted.



(c)  $\alpha = 14.4^\circ$



(d)  $\alpha = 18.4^\circ$

— Theory (Ref. 1)

○ Experiment

Note: 1. Separation predicted at  $.89c$  for  $\alpha = 14.4^\circ$ ,  $.830c$  for  $\alpha = 18.4^\circ$ .  
 2. SX Experimental separation point.

Figure 20 - Concluded.

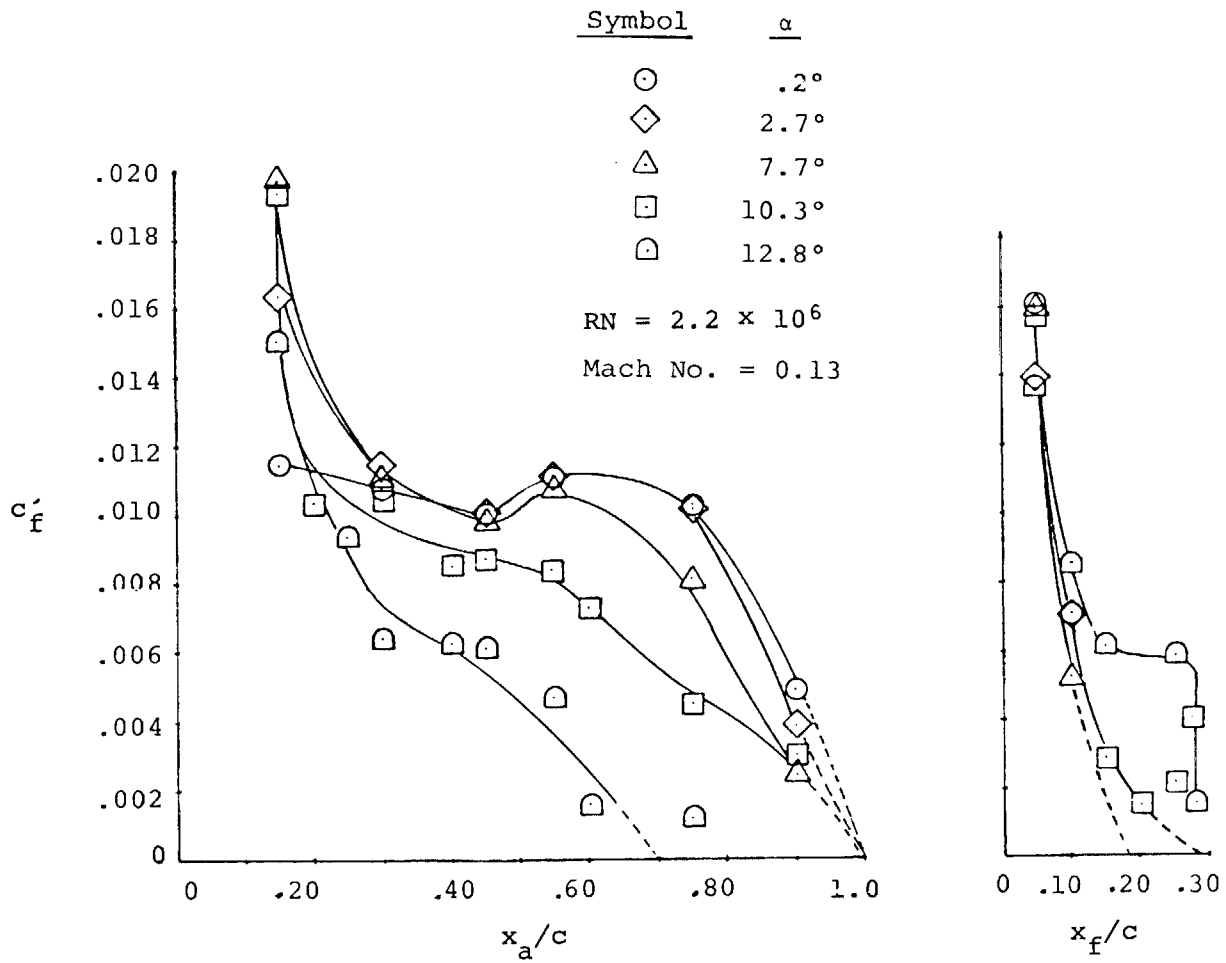


Figure 21 - Local Skin Friction Distributions.  $\delta_f = 40^\circ$ , Optimum gap.

